Experimental study of realistic low–noise technologies applied to a full–scale nose landing gear

Roberto Merino-Martínez [a],[*], John Kennedy [b], Gareth J. Bennett [b]

[a] *Faculty of Aerospace Engineering, Delft University of Technology, Kluyverweg 1, 2629 HS Delft, the Netherlands*
[b] *Department of Mechanical and Manufacturing Engineering, Trinity College Dublin, Ireland*

A B S T R A C T

The landing gear system is the dominant airframe noise source for most modern commercial aircraft during approach. This manuscript reports the results from the ALLEGRA (Advanced Low Noise Landing (Main and Nose) Gear for Regional Aircraft) project. This project assessed the performance of several highly realistic low–noise technologies (LNTs) applied to a detailed full–scale nose landing gear (NLG) model in aeroacoustic wind–tunnel experiments. Four individual low–noise concepts tested, namely a ramp door spoiler, a solid wheel axle fairing, wheel hub caps, and multiple perforated fairings. Combinations and small variations of some of these LNTs were also evaluated. The use of multiple planar microphone arrays allowed for the application of 2D and 3D acoustic imaging algorithms to assess the location and strength of the noise sources within the NLG system in different emission directions for each configuration. The wheel axle, the inner wheel hubs, the steering pinions and the torque link were identified as the noisiest NLG elements. The solid wheel axle fairing was the most effective individual LNT, and it improved its performance when applied in combination with the ramp door spoiler and wheel hub caps, reaching overall noise reductions of more than 4 dBA.

1. Introduction

Noise emissions generated by aircraft cause severe annoyance to tens of millions of people living in the vicinity of airports and pose environmental constraints for airport operations, with the consequence of revenue loss. The successful development of low–noise propulsion technologies has increased the significance of airframe noise in modern commercial aircraft [1]. Hence, in order to fulfil the ambitious aircraft noise reduction requirements set by governmental organisations, such as ACARE [2] (Advisory Council for Aviation Research and Innovation in Europe), and projects such as Flight Path 2050 [3], airframe noise levels need to be further reduced, as they set the threshold to aircraft noise in the future [4,5].

With respect to environmental noise, the landing gear (LG) system is often the dominant airframe noise source during approach and landing [6–8] depending on the aircraft. A typical LG system consists of complicated structures of bluff bodies (struts, links, wheels, tires, fairings, etc.) of considerably different sizes. Because of its critical importance for the aircraft's safety, this system has little aerodynamic and aeroacoustic refinement to ease its inspec-

tion and maintenance, which are essential to the reliability of the LG [9]. As such, aerodynamic noise is produced when interacting with the surrounding airflow [9]. The bluff body components of the landing gear radiate noise directly [10] and noise is also generated by the subsequent interaction of turbulent wake flow with down-stream located gear elements [11]. In addition, research projects continue to examine the seemingly ever present problem of tonal cavity noise in landing gears of commercial aircraft [12–14], initially identified as an issue several decades ago [10,15].

Depending on their size, LG elements are normally divided into three categories [16,17]:

1. **Large–scale structures** such as the wheels and the wheel bay, which contribute to the low–frequency noise.
2. **Mid–scale structures** such as the main struts, which contribute to the mid–frequency noise.
3. **Small–scale structures** such as the hydraulic lines, wires, and LG dressings, which contribute to the high–frequency noise.

Research to date has attempted to measure the contributions of some of these components to form a basis for semi–empirical airframe noise prediction models [6,16–19] and the design of LG low–noise technologies (LNTs) [20]. Because of their nature, such semi–empirical prediction models have limited reliability when

* Corresponding author.
E-mail address: r.merinomartinez@tudelft.nl (R. Merino-Martínez).

estimating the performance of LNTs or unconventional LG designs [5]. Therefore, dedicated experimental research is required for evaluating and validating the potential noise reductions that these LNTs can provide. The findings from such studies would provide valuable information on the noise generation mechanisms and low−noise design criteria for future and improved LNTs. Previous studies [21,22] showed that the high−frequency noise emissions of LGs are a significant contributor to the overall sound pressure level ($L_{p,overall}$) and, therefore, in order to properly represent them, it is essential to employ highly detailed and ideally full scale models in wind−tunnel experiments and in computational simulations [5,20].

The current study employs the full−scale nose landing gear (NLG) model from the ALLEGRA (Advanced Low Noise Landing (Main and Nose) Gear for Regional Aircraft) project [23−26]. This included a full representation of the NLG details and associated structures (e.g., wheel bay cavity, bay doors, fairings, nose fuselage and hydraulic dressings). One of the additional benefits of manufacturing the accurate nose fuselage in the test campaign, as well as to house the wheel bay, was to provide the correct boundary layer and aerodynamic flow field, resulting from the associated curvatures, to impinge upon the NLG. This unusual level of detail was intended to bring the wind−tunnel tests closer to the conditions experienced in real flight.

Several LNTs for decreasing the sound levels emitted by the LG system have been investigated in the last decades. In general, LNTs for the LG system aim at reducing the incoming flow velocity, suppress cavity resonance, shield small components, or prevent wake interactions [9]. They can be grouped into four categories depending on how they function: component enhancement, component smoothing, flow enhancement, and flow deflection. Whereas the design optimization of certain LG components (such as the wheel spacing, boogie angle, leg−door structure, and brakes) has been evaluated in projects such as SILENCER [27] and TIMPAN (Technologies to Improve Airframe Noise) [28], the use of noise abatement treatments as passive add−ons (such as fairings, spoilers, caps, and optimized components) is considered as the simplest retrofit technology approach to noise reduction for existing gear designs [29]. Considerable work has been devoted in the last years to the study of active noise reduction devices as well, such as air curtains [30,31] or plasma actuators [9], but their technology readiness level (TRL) is relatively low to date. A good overview of most LNTs developed to date is presented in [9].

The objective of the present research is to assess the performance of four realistic LNTs applied, individually, in certain combinations, and with variations, to a NLG model in aeroacoustic wind−tunnel measurements: a ramp door spoiler, a wheel axle wind shield, wheel hub caps, and a perforated fairing. These technologies were selected based on criteria, such as their potential noise reduction, weight, cost, ease of implementation, TRL, and operational and maintenance impact. These LNTs have a medium to high TRL and are suitable for flight testing and commercial implementation in the near term in the early 2020s.

Phased microphone arrays and acoustic imaging techniques are normally employed for estimating the location and strength of the sound sources [32−34] and to isolate their contributions. This approach has been previously used in studying landing gear noise in flyover measurements [35−38] and wind−tunnel experiments [25,26,39,40]. In the ALLEGRA wind−tunnel experimental campaign, several microphone arrays were used synchronously to measure the NLG noise emissions, which the authors have identified as an opportunity for 3D acoustic source mapping [41]. Henceforth, this approach is employed for studying the three−dimensional location and strength of the noise sources within the NLG model, and how the LNTs influence these.

The paper is structured as follows. Section 2 describes the experimental facility utilised, as well as the NLG model and the LNTs
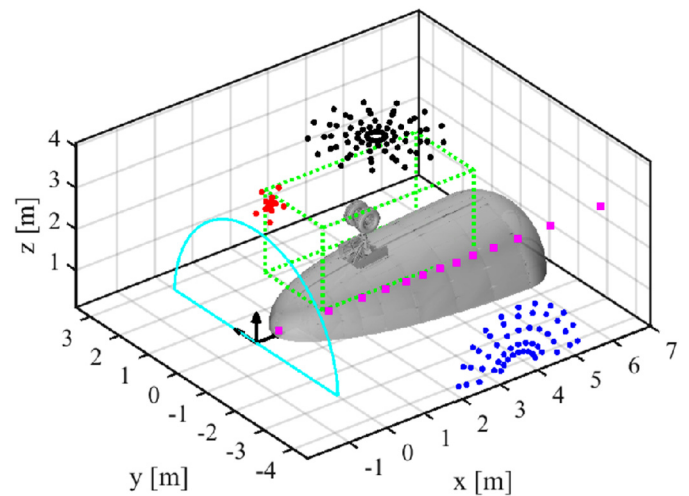
Fig. 1. Scheme showing the ALLEGRA NLG model placed inside the Pininfarina wind tunnel, the coordinate system, the four microphone arrays (denoted as black, blue, red, and magenta dots, respectively), the wind−tunnel's nozzle exit plane (in cyan) and the limits of the scan grid selected (in green). The flow moves in the positive *x* direction. (For interpretation of the colours in the figure(s), the reader is referred to the web version of this article.)

considered. The acoustic imaging methods employed for the three−dimensional source mapping and the quantification of the noise levels are briefly explained in section 3. The results obtained are discussed in section 4, whereas the main conclusions are gathered in section 5.

2. Experimental setup

2.1. Wind−tunnel facility

The experimental measurements were performed in the Pininfarina open−jet, semi−cylindrical wind−tunnel facility in Turin, Italy, which has a test section of 8 m (length) × 9.60 m (width) × 4.20 m (height). The semi−circular nozzle has a diameter of 5.64 m [42]. The facility is equipped with a low−noise, high−speed fan−drive system consisting of 13 fans, which provides flow velocities up to 72.2 m/s. For this study, flow velocities U_{∞} of 40 m/s, 50 m/s, and 60 m/s were considered, providing a maximum Mach number of about 0.18. The background noise for the ALLEGRA NLG tests was a considered as a combination of the wind−tunnel noise and the noise produced by the fuselage itself with the bay cavity sealed. Both are mostly low−frequency noise sources (below 100 Hz), outside of the frequency range of interest in this paper. The reader is directed to a separate study which focuses on low−frequency wheel bay noise [13]. The addition of the NLG causes an increase in the noise levels between 5 and 12 dBA across a very wide frequency range [24]. The flow velocity produced by the wind tunnel is very uniform, since it varies by only 0.5% over the test area. The turbulence intensity level had a value of approximately 0.3% in these experiments.

Fig. 1 depicts the relative position of the NLG model in the wind tunnel, as well as the coordinate system employed, where the *xz* plane is the symmetry plane of the test model, the *yz* plane corresponds to the wind−tunnel nozzle exit and the origin is situated on the floor of the testing platform (*xy* plane). The NLG complete model, with the partial fuselage, was placed in the wind tunnel so that the distance between the wind−tunnel's nozzle exit plane and the NLG wheel axis was 2.8 m. The wind−tunnel's shear layer was measured and it was confirmed that it did not impinge on the test model for any of the flow velocities considered. The coordinates of the middle point of the wheel axis were:
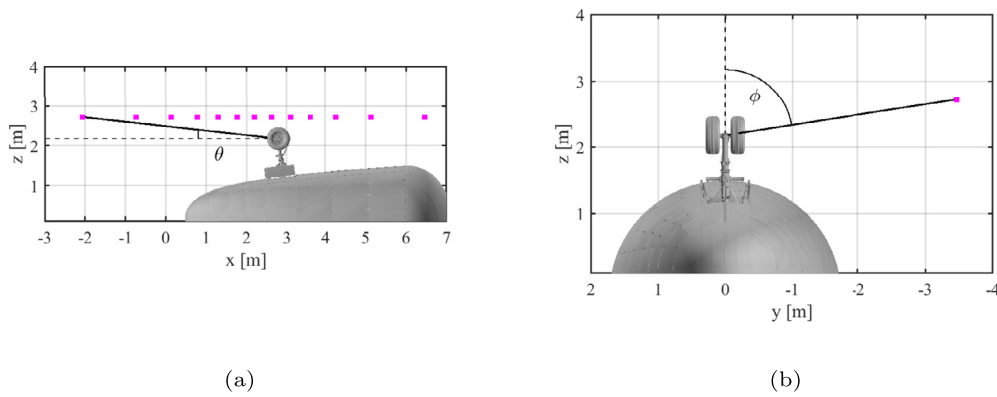
(a)   (b)

Fig. 2. Location of the side linear array and emission angles with respect to the middle point of the wheel axis of the NLG model. The flow moves in the positive *x* direction.

$$x = 2.8 \text{ m}; \quad y = 0 \text{ m}; \quad z = 2.175 \text{ m}.$$

Henceforth, two different angles are employed for defining the direction of the noise emissions of the NLG model with respect to the coordinates of the middle point of the wheel axis: (1) the polar emission angle θ with respect to the expected flight direction, with $\theta = 0°$ in the upstream direction, $\theta = 90°$ in the *flyover* direction (i.e. in the positive *z* direction), and $\theta = 180°$ in the downstream direction, see Fig. 2a; and (2) the azimuthal emission angle ϕ, with $\phi = 0°$ in the *flyover* direction (i.e. in the positive *z* direction) and $\phi = 90°$ in the lateral right direction (i.e. in the negative *y* direction), see Fig. 2b.

Four different planar microphone arrays were installed at the top, side and front of the wind tunnel outside of the flow. For the present study, data from all arrays were used:

1. For considering the acoustic emissions radiated in the *flyover* direction (i.e., for polar emission angles $\theta \approx 90°$) the top array was employed (illustrated in Fig. 1 with black dots). The array consisted of 78 microphones in a multi–arm spiral arrangement of approximately 3 m diameter. This array was located in the $z = 4$ m plane, i.e., at a distance to the NLG wheel axis of 1.825 m.
2. To study the lateral or *side* emission pattern of the NLG (i.e., for azimuthal angles $\phi \approx 90°$) the side array was used (see blue dots in Fig. 1). The array was positioned in the $y = -4.22$ m plane, i.e. parallel to the model plane of symmetry and consisted of 66 microphones arranged in a half–wheel distribution with a diameter of approximately 3 m.
3. A spiral *front* array consisting of 15 microphones was placed upstream the NLG forming an angle of 10° with the *yz* plane (see red dots in Fig. 1).
4. Lastly, a side linear array of 13 microphones on the same side and at the same horizontal distance from the model axis as the *side* array. These microphones are depicted as magenta dots in Fig. 1. Fig. 2 illustrates the emission angles from the middle point of the NLG wheel axle that can be measured by the side linear array, including a single azimuthal sideline angle ϕ of 81° and polar emission angles (with respect to the expected flight direction) θ covering a range from approximately 6° to 171°. The shear layer caused by the flow motion inside the open–jet wind tunnel requires velocity–dependent geometrical corrections, that limit the effective measurable range of emission angles [32].

The data of all microphones was acquired simultaneously at a sampling frequency of 32,768 Hz for 10 s per measurement. The time–averaged cross–spectral matrices (CSMs) [43] were obtained by using frequency spectra processed with a block length of 8192 samples (0.25 s), Hanning windowing and 50% data overlap, providing a converged solution with a frequency resolution Δf of 4 Hz.

The frequency range of interest selected for postprocessing extends from 200 Hz to 4000 Hz. The lower limit was defined by the background noise and the spatial resolution of the array in order to properly separate the sound coming from the NLG model from other noise sources. The higher frequency limit was imposed by the minimum distance between microphones to prevent aliasing, the amount of sidelobes, and the signal–to–noise ratio.

For additional details about the experimental setup, the reader is referred to [44].

2.2. Nose landing gear (NLG) model

The full–scale NLG model used in the ALLEGRA project included a full representation of the NLG details and associated structures (e.g., bay cavity, bay doors, nose fuselage and hydraulic dressings). This LG geometry is that of an advanced regional turboprop aircraft design and was provided to the authors by members of the Clean–Sky consortium [23]. The diameter and width of the NLG tires were 0.577 m and 0.221 m, respectively, and the rim diameter was 0.286 m. The separation between wheels was 0.159 m. The main strut had a length of 1.295 m and an average diameter of 0.11 m. Additional details on the geometry can be found in the thesis of Neri [44].

Fig. 3 shows a picture of the model inside the wind tunnel. The nose fuselage had a streamwise length of 6.697 m and a maximum width in the *y* direction of 3.417 m. The height of the model, combining the fuselage and NLG model, was 2.463 m.

The wind–tunnel model had a fixed, built–in angle of attack of 4°. Each model configuration was tested for a range of flow speeds and yaw angles ($\pm 5°$ and $\pm 10°$), allowing the analysis of conditions equivalent to landing with crosswind [44]. For this paper, only the yaw angle of 0° (no crosswind) was considered.

Fig. 4 identifies the principal components that can generate noise on a schematic of the ALLEGRA NLG. The baseline configuration is considered to be the extended landing gear with hydraulic dressing applied and is referred to as test case NLG.

Henceforth, the NLG baseline configuration is referred to as NLG–BASE, see Table 1. The configuration with only the fuselage (with the bay cavity sealed and without the NLG present) is denoted as NLF and it was used as a reference to calculate the wind–tunnel's background noise levels. An additional configuration without the hydraulic dressings was tested and referred to as NLU. A component noise assessment on the baseline configuration was performed by Bennett et al. [24] and reported high–amplitude bay cavity resonance modes at frequencies below 100 Hz, especially in the *flyover* direction [13].

Fig. 3. ALLEGRA NLG model inside the wind tunnel with the top array visible. The view direction is from upstream towards downstream [44].
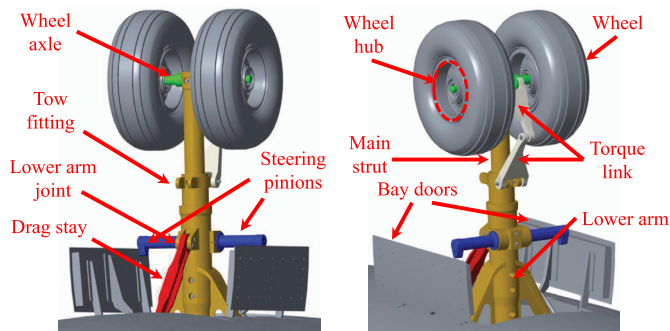
Fig. 4. Principal components on the NLG model as seen from upstream (left) and downstream (right).

2.3. Low–noise technologies (LNTs)

This paper reports on four different LNTs, which included multiple separate approaches to noise reduction. These technologies are applied individually and in certain combinations and variations to the NLG model with hydraulic dressing (i.e. the NLG–BASE configuration). The main characteristics of the LNTs considered are summarised in Table 1. Some photographs of the NLG model with the four LNTs are presented in Fig. 5.

A brief description of each of the LNTs considered is provided below:

1. The first LNT considered was a retractable ramp door spoiler (denoted as NL1) placed upstream of the bay cavity, see Fig. 5a, which causes a deflection of the flow onto the outer regions of the extended gear. Its main objective is to mitigate the bay cavity noise generation mechanisms and to shield the steering pinion, drag stay, lower arm, upper strut, and bay doors from the incoming flow. However, the potential deflected flow interaction with the front edge of the wheel bay doors may generate new noise sources, as well as the flow separation from the trailing edge of the ramp door spoiler [9]

Table 1
ALLEGRA low–noise technologies.

Test ID	Fuselage	Landing gear	Low–noise technology
NLF	Sealed	None	None
NLU	Open Bay	Undressed	None
NLG–BASE	Open Bay	Dressed	None
NL1	Open Bay	Dressed	Ramp door spoiler
NL2	Open Bay	Dressed	Solid wheel axle fairing
NL3	Open Bay	Dressed	Wheel hub caps
NL4	Open Bay	Dressed	Multiple perforated fairings
NL5	Open Bay	Dressed	NL2 + NL3 + NL4
NL6	Open Bay	Dressed	NL1 + NL2 + NL3
NL7	Open Bay	Dressed	NL4 with alternative material
NL8	Open Bay	Dressed	NL4 only applied to the wheel axle

and the interaction of its wake with the leg. The primary benefits of this LNT are expected to be observed for low frequencies (below 300 Hz).

2. The second LNT employed (NL2) was a wheel axle wind shield solid fairing, see Fig. 5b, whose function is mainly to deflect flow and produce a more aerodynamic and, hence, quieter geometry. This LNT has probably the highest TRL due to several previous experiments, even in real flight scenarios [9,20]. This LNT is expected to effectively mitigate the relatively strong noise source between the wheels which has been identified in previous studies [20,24,45]. In addition, this fairing design, was designed to allow for wheel deformation during touchdown. Due to the design of the aircraft, there were no brakes in the NLG, which allows for the location of such a large fairing. Such a solution would typically not be possible for an MLG, however, as its presence would compromise the convective cooling required for its brakes. With regards to the NLG, a potential penalty for this LNT is the generation of low–frequency noise (below 300 Hz) due to the flow deflection to adjacent and downstream uncovered gear components [9]. In addition, the relatively large fairing size may also cause vortex shedding.

3. The NL3 treatment consisted of both inner and outer wheel hub caps (see Fig. 5c to cover wheel hub voids and, hence, reduce the noise caused by the interaction of the air and the wheel [46,47]. The inner hub caps are possible due to the lack of brakes in the NLG design, but this LNT is expected to be easily installed and to have a negligible impact in the landing gear operation [9]. Tire deflection was taken into account in the detail of their design.

4. The fourth case, NL4, was a perforated fairing design covering multiple regions of the NLG (lower arm, the steering pinion and wheel axle in Fig. 4), see elements highlighted in blue colour in Fig. 5d. Compared with solid fairings (such as NL2), porous fairings with correctly designed porosity, reduce the velocity of the deflected flow towards the fairing's sides and the vorticity generated [9]. In addition, they are expected to have a lower weight and benefits on brake cooling [48]. On the other hand, they are expected to cause high–frequency noise due to the shearing flow past the perforations, although correct design can push these frequencies above the threshold of hearing. It should be noted that the wheel axle solid fairing of NL2 was larger than that of NL4. More information about the properties of the perforated material is provided in section 2.3.1.

These four LNTs affect a range of areas and components of the NLG system and, as such, may be applied either in isolation or in combination. Two combination technologies which included a
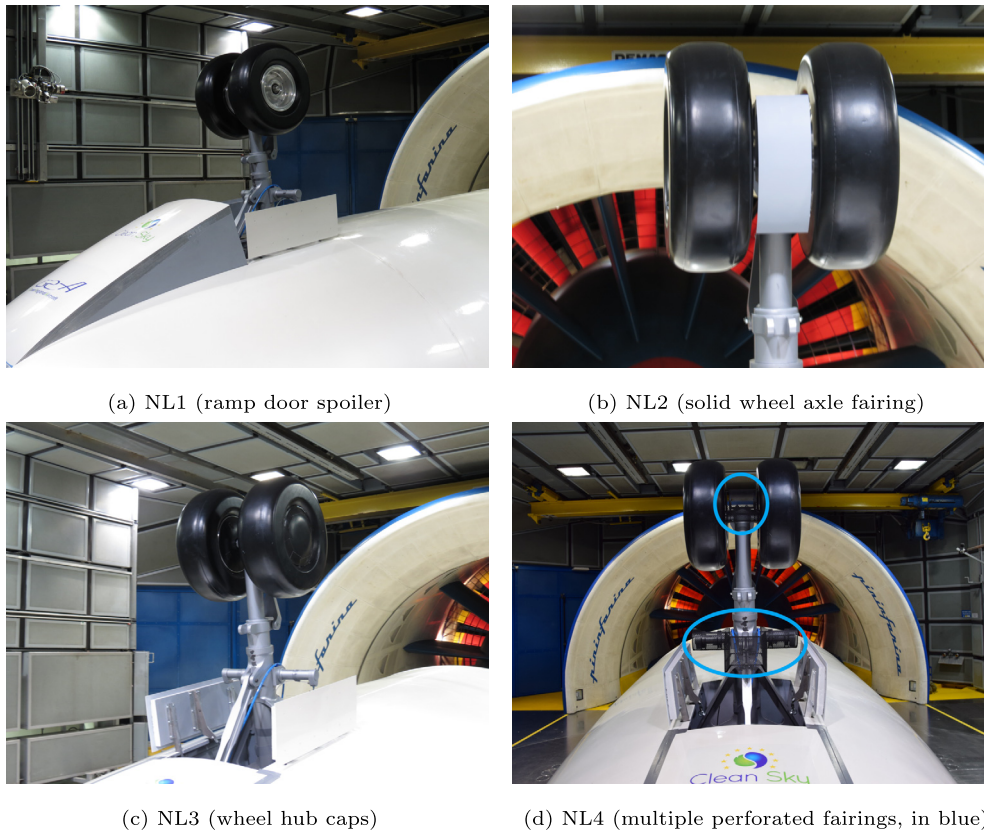
(a) NL1 (ramp door spoiler)

(b) NL2 (solid wheel axle fairing)

(c) NL3 (wheel hub caps)

(d) NL4 (multiple perforated fairings, in blue)

Fig. 5. Photographs of the NLG model fitted with LNTs inside of the wind–tunnel.

subset of three of the individual technologies were tested, referred to as:

5. NL5, which was a combination of NL2, NL3, and NL4. In or-der to allow for the combination of these technologies to be tested, the wheel axle fairing of NL4 was excluded due to the identical placement of the component with the NL2 technol-ogy, i.e. only the elements highlighted by the lower blue oval in Fig. 5d were present.
6. NL6, which was a combination of NL1, NL2, and NL3. This LNT addresses the noise sources on the steering pinions, leg struc-ture, wheels, and bay doors.

Furthermore, two additional LNTs were tested with different perforated fairing characteristics:

7. The technology NL7 consisted of the same fairing locations and dimensions of NL4 but with an alternative perforated material, see section 2.3.1 and Fig. 6b.
8. Since no direct comparison could be made between NL2 and NL4, because NL4 also included fairings in other locations on the gear, a configuration which included just the wheel axle component (the elements highlighted by the higher blue oval in Fig. 5d) of the perforated fairing with the same mate-rial as NL4 was included in the test campaign, referred to as NL8.

Whereas all of the selected LNTs were considered to be at a medium to high TRL this does not mean that all their design con-siderations are complete, and certain considerations can still be optimized, such as the consequent added weight, their influence on the aerodynamic performance (i.e. a potential drag increase), brake cooling, and structural stability of the NLG [49]. Moreover,

these LNTs should be compatible with the safety regulations and not hinder the inspection and maintenance procedures. Lastly, it should be noted that, although some of these LNTs have been relatively successful in wind tunnel measurements [21,27,28,50], careful considerations need to be taken for scaling–up wind–tunnel results to flight tests with actual aircraft [20,51–54], such as instal-lation effects.

2.3.1. Perforated fairings

One of the key parameters when designing perforated fairings is the porosity of the material. The noise reductions achievable by porous materials greatly depend on their porosity [48,55]. The percentage porosity σ of a perforated plate of circular holes with triangular pitch depends on the diameter d the pitch p, see Fig. 6a, and is defined as [56]:

$$\sigma = 100 \, \frac{\sqrt{3}\pi}{6} \left(\frac{d}{p} \right)^2 \tag{1}$$

The aerodynamic and acoustic characteristics of a perforated material strongly depend on the geometry of the perforate. Thus, it is possible to design and optimize a perforated material for the desired aeroacoustic performance. Boorsma et al. [56,57] defined a set of guidelines to be followed when applying perforations to LG fairings. It was reported that perforated fairings had the potential to break down large–scale flow structures such as vortices, which are a negative consequence of using solid fairings (such as NL2), hence considerably reducing the broadband noise levels, including the fairing self–noise. However, values of porosity which were too high were shown to allow too much fluid to be bled through, thus recreating a noise source at the LG strut itself. The self–noise of a perforated material is influenced by the mass flow through the
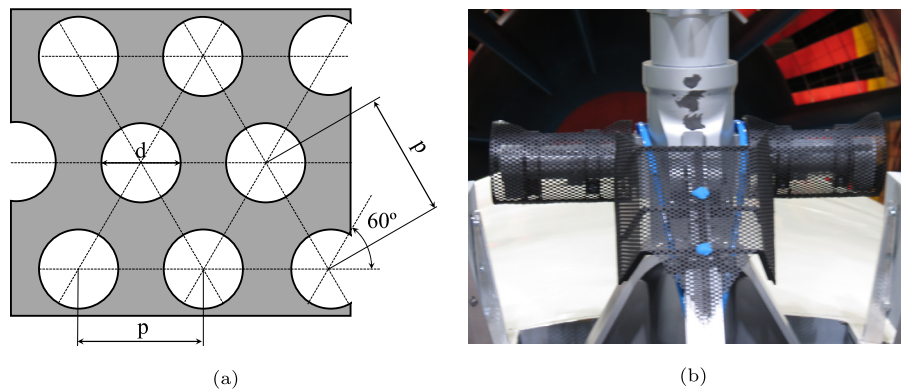
Fig. 6. (a) Explanation of the parameters defining the perforated meshes considered. (b) Detail of the perforated fairing around the drag stay for NL7 (with $\sigma = 40.31\%$).

Table 2
Perforated material properties for the NL4 and NL7 test cases.

	NL4	NL7
σ	29.61%	40.31%
p	3.5 mm	6 mm
d	2 mm	4 mm

holes. While this is dependent on the flow speed, there is also a dependency on the hole size [55]. It was suggested that a pore diameter of less than 3 mm would generate noise outside the audible range for approach conditions [56,57]. Boorsma et al. [56,57] applied a fairing with a porosity of 40% to a LG model for wind–tunnel tests. In the context of ALLEGRA, the two materials available met one, but not both of these conditions of small hole sizes and relatively high porosity. The NL4 case consisted of the smaller 2 mm hole size, but with a lower porosity of 29.6% whereas the NL7 case consisted of a larger hole size, 4 mm, with a higher porosity of 40%. Both perforated meshes had a thickness of 1 mm and a pitch angle of 60°, see Fig. 6a. The material properties are given in Table 2.

These two porous materials were selected based on input from the Clean Sky GRA members, manufacturing considerations, a literature review [56,57] and small–scale tests completed prior to the wind–tunnel test campaign. The literature review suggested an improved performance for a greater porosity with a high frequency penalty which is a function of the hole size. For practical aircraft applications, an appropriate material selection is required due to the arduous working environment [9].

3. Acoustic imaging method

The data recorded by the microphone arrays was employed for the application of both two– and three–dimensional acoustic mapping algorithms. In all cases, the main diagonal of the CSM was removed in order to eliminate the influence of noise incoherent for all the microphones [36], such as the wind noise. The convection of the sound waves due to the flow velocity was considered and a standard shear layer correction, as described by Amiet [58], was applied. In addition, a weighting function was applied to minimize coherence loss, especially for outer microphones and at high frequencies [33].

3.1. Two–dimensional acoustic mapping

Conventional frequency domain beamforming (CFDBF) [33] was applied to the acoustic data acquired by the top and side microphone arrays, separately, in order to obtain the 2D acoustic source maps in the xy and yz planes, respectively. For each point in a defined scan grid, CFDBF estimates the agreement between the recorded pressures by the microphone array and the pressures for a modeled sound source according to the radiation model selected by the user (typically an omnidirectional monopole). This technique is widely used for source mapping, since it is robust, fast, and intuitive [59].

Hence, a scan grid needs to be defined that contains the expected location of the sound sources. For the top array, a square scan grid at the plane containing the NLG axis ($z = 2.175$ m) was defined, ranging from $x = 2$ m to $x = 4$ m and from $y = -1$ m to $y = 1$ m. The side array employed a square scan grid in the symmetry plane of the NLG (i.e. $y = 0$ m) that extended from $x = 2$ m to $x = 4$ m and from $z = 1$ m to $z = 3$ m. Both scan grids have a spacing between grid points of 0.01 m, i.e. a total of 40, 401 grid points. Employing a 2D grid for a three–dimensional sound source, such as a NLG, is a simplification, but the results obtained when considering other scan planes showed essentially the same values.

A region of integration (ROI) covering the NLG position was defined for each microphone array case, following the approach of the Source Power Integration technique (SPI) [36,60,61]. The integrated acoustic power within the ROI was then normalized by the integrated array response for a point source in the centre of the ROI, also known as Point Spread Function (PSF). In such a way, more physical results can be obtained, because the influence of the array's geometry in the L_p results is reduced [36,61] and the source maps are brought back to a single sound pressure level L_p. The ROI for the source maps calculated in the *flyover* emission direction extended from $x = 2.3$ m to $x = 3.3$ m and from $y = -0.5$ m to $y = 0.5$ m, and for those in the *side* direction from $x = 2.3$ m to $x = 3.3$ m and from $z = 1.1$ m to $z = 2.6$ m. These ROIs were selected to cover the noise sources on the NLG model, see Figs. 7 and 8.

Additionally, the enhanced high–resolution deconvolution method EHR–CLEAN–SC [62–64] was also applied to the data from both arrays in order to obtain a better dynamic range (fewer and lower sidelobes, i.e. spurious sources) and to investigate whether one or multiple sound sources were present (even beyond the Rayleigh resolution limit [62,63]). The loop gain [62] selected was 0.9 and the number of sound sources considered was estimated based on the number of dominant eigenvalues of the CSM for each frequency case [59]. The width of the synthetic *clean* main lobes has to be input by the user and, in this case, a large enough width was selected to ensure a clear visualization. For the frequency range considered (200 Hz to 4 kHz), the differences between the obtained spectra by the SPI technique and EHR–CLEAN–SC were relatively small. Henceforth, the spectra obtained with EHR–CLEAN–SC are presented in this paper.

(a) NLG–BASE (b) NL1 (c) NL2

(d) NL3 (e) NL4 (f) NL5

(g) NL6 (h) NL7 (i) NL8
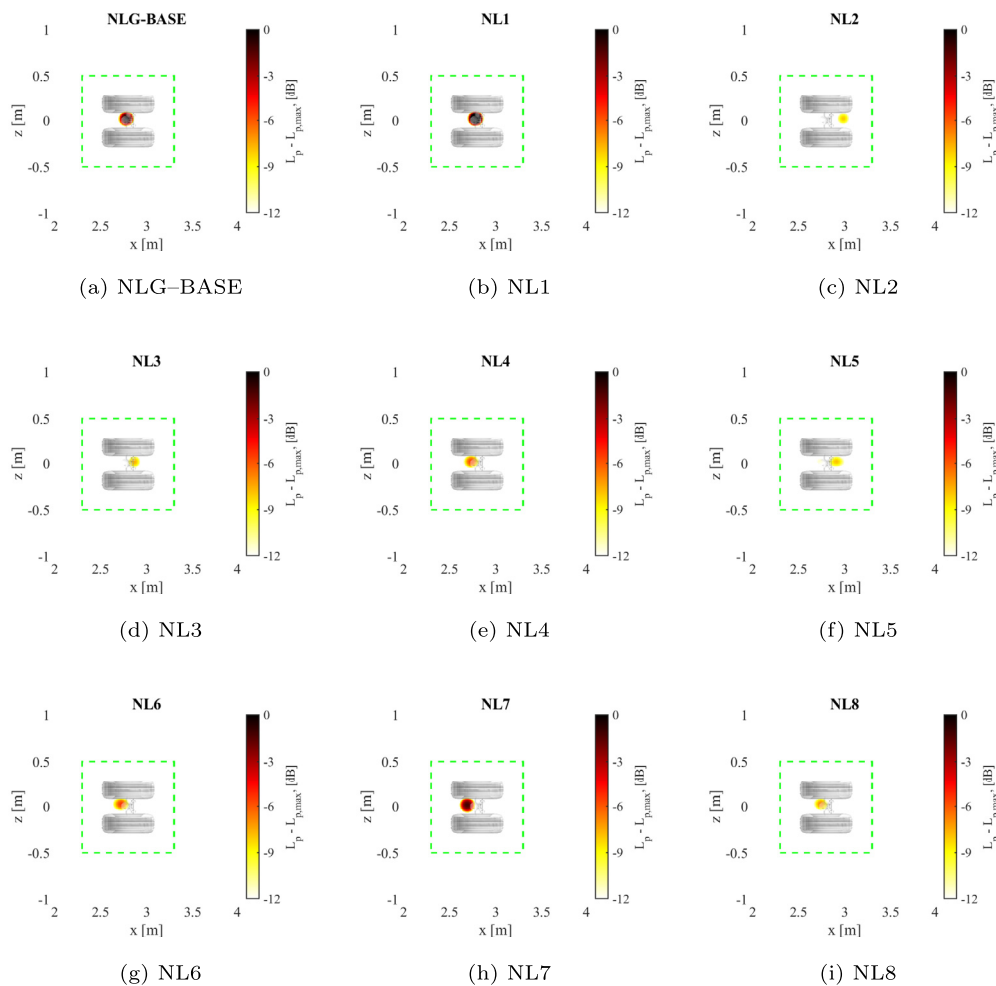
Fig. 7. EHR–CLEAN–SC source maps for the *flyover* direction for a one–third–octave–band centred at 1250 Hz and $U_\infty = 50$ m/s. The reference case NLG–BASE is shown in subfigure (a) and subfigures (b–i) correspond to the cases NL1–NL8, respectively. The ROI is denoted as a dashed green rectangle.

3.2. Three–dimensional acoustic mapping

In order to obtain more precise information about the spatial location of the noise sources for each of the NLG configurations described in Table 1, CFDBF and EHR–CLEAN–SC were applied to a three–dimensional scan grid that contained the NLG and ranged from $x = 1$ m to $x = 4$ m, from $y = -1$ m to $y = 1$ m, and from $z = 1$ m to $z = 3$ m (see the volume limited by green dashed lines in Fig. 1). The three–dimensional scan grid also had a spacing between grid points of 0.01 m, i.e. a total of $12,160,701$ grid points. As for the 2D case, the widths of the *clean* main lobes of EHR–CLEAN–SC were selected to be relatively large to ease the visualization.

The advanced experimental setup, with several microphone arrays on different planes (i.e. with different points of view) is beneficial for using 3D acoustic mapping [41,65]. Instead of using all the microphones synchronously as a larger array, the 3D source maps obtained, respectively, by the top, side, and front arrays separately were calculated and then combined into a total 3D source map using a multiplicative approach. For each scan point the geometric average of the source autopowers in the 3D source maps obtained by each of the three arrays was calculated (i.e. the cubic root of the product) [41,65]. In that way, the different sidelobe patterns of each array are averaged out, since these strongly depend on the relative position between the sound source and the microphone array. Porteous et al. [41] showed that better results were obtained when using this technique compared to simply us-

ing all the available microphones simultaneously. The beamforming formulation has to be adapted accordingly for obtaining the correct source locations in 3D [66]. Battista et al. [67] employed inverse methods and CLEAN–SC for three–dimensional acoustic source mapping of an aircraft model using the same microphone arrays in the same wind tunnel, and suggested that the use of multiple arrays is preferred when source localization accuracy is crucial. However, it was argued that excessive source directivity or potential shielding of the sound emissions in certain directions may deteriorate the localization, but specially the quantification of noise sources using this approach [67]. In the current setup, for example, a noise source located between the wheels would not be directly visible to the side array. Therefore, 3D acoustic source maps are difficult to directly interpret to obtain quantitative results. Hence, for the present research, 3D acoustic source mapping is only employed for source localization, and the quantification of the noise emissions in the *flyover* and *side* directions is performed by integrating the 2D ROIs defined in section 3.1.

The 3D acoustic source maps presented henceforth depict isocontours of the grid points that have a L_p below a certain threshold in dB below the peak value within the map.

4. Results

As discussed, the study presented in this article continues the analysis of data from the ALLEGRA test campaign. With respect to the NLG results, the outcome of the work published by Ben-
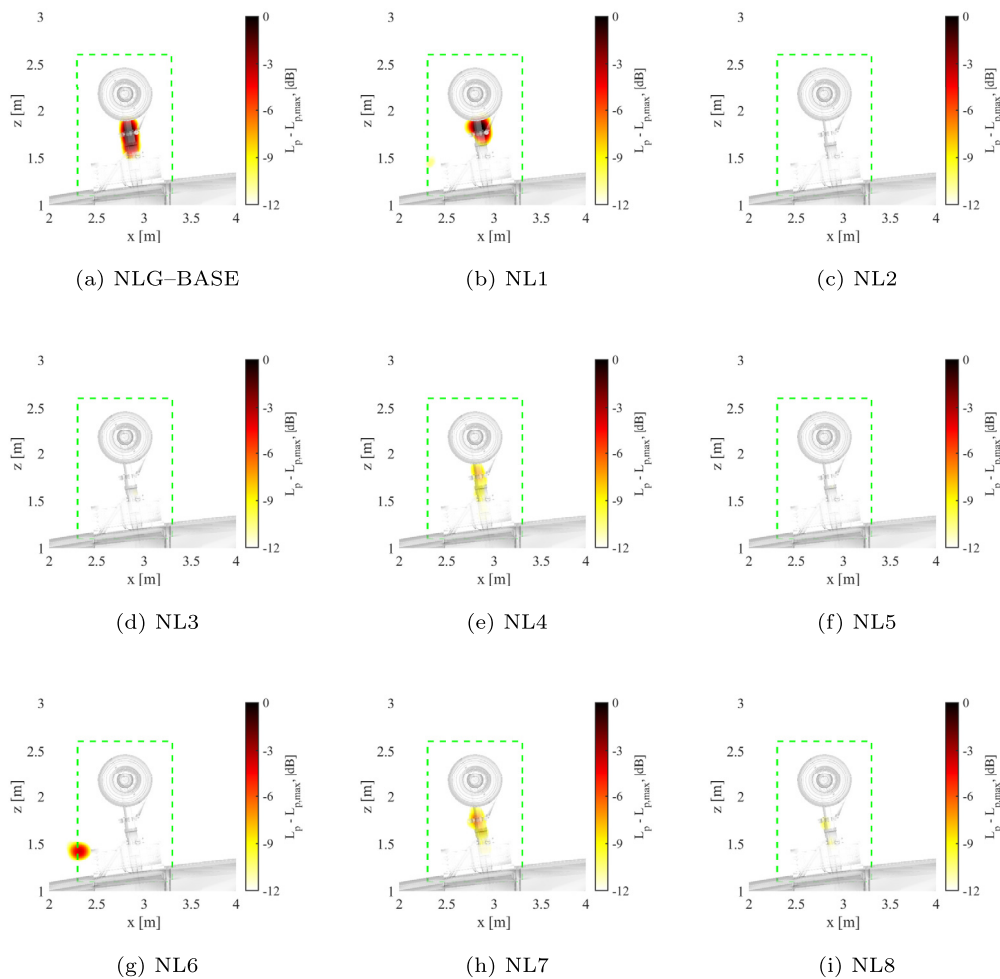
Fig. 8. EHR–CLEAN–SC source maps for the *side* direction for a one–third–octave–band centred at 1250 Hz and $U_\infty = 50$ m/s. The reference case NLG–BASE is shown in subfigure (a) and subfigures (b–i) correspond to the cases NL1–NL8, respectively. The ROI is denoted as a dashed green rectangle.

nett et al. [24] and Neri et al. [13] resulted in certain conclusions. The first was that the presence of the bay, doors, and dressed NLG increased the noise levels over the NLF configuration (closed bay fuselage with no leg) by up to 15 dB as measured by microphones in the linear array. The majority of the noise increase was measured in the 200 Hz to 1 kHz frequency range with the most significant increases centred around 200 Hz and 350 Hz with a bias in directivity towards to forward arc. A second key conclusion was that significant noise can be generated in the wheel bay below 200 Hz due to the shear layer excitation over the bay cavity, but that these Helmholtz–resonance and duct mode noise sources tend to be attenuated by the presence of the leg and doors. With specific focus on the noise generated by the NLG wheels, a third set of conclusions found that the wheels generated noise in the 315 Hz, 630 Hz and 1.25 kHz one–third–octave bands, with the latter two frequency ranges being shown to result from inter–wheel noise sources. It was also shown in Bennett et al. [24], that adding hub caps (internal and external) was as effective at reducing the noise level as simply removing the wheels entirely.

4.1. Two–dimensional results

4.1.1. Two–dimensional source maps

This section contains some illustrative examples of 2D acoustic source maps obtained by the top and side arrays, used separately. These source maps are employed to obtain information about the location of the main noise sources within the NLG model and to

quantify the noise levels emitted by integrating them over a ROI, as explained in section 3.1. Only the results with the flow velocity $U_\infty = 50$ m/s are reported for reasons of brevity and to allow for comparisons with the results to be found in previous publications [13,24–26]. Results corresponding to the one–third–octave frequency band centred at 1250 Hz are presented, as LNTs were found to dramatically reduce noise in this frequency band, as will be seen in Figs. 10 and 12. The source maps are plotted over a cutout of the NLG 3D model at the location of the scan plane (see grey contours in Figs. 7 and 8). Unfortunately, the 3D models of the LNTs were not available, so the 3D NLG model corresponds to the baseline case (NLG–BASE). Lastly, the L_p values shown are relative to the maximum value of the reference case (NLG–BASE) and all 2D source maps have a dynamic range of 12 dB.

Fig. 7 depicts the source maps obtained by the top array for the 1250 Hz case for the baseline case (NLG–BASE) and the eight LNTs. As is usually the case with flyover angle beamforming [68], this point of view does not provide precise information on the location of the strongest noise sources. The baseline case (Fig. 7a) shows a main noise source located at the middle point of the wheel axle, that could just as easily be located along the main strut. A similar source distribution was observed by Yokokawa et al. [20] in a comparable experiment. The largest noise reduction for this example is achieved by NL2 (solid wheel axle fairing, see Fig. 7c), showing a reduction of the peak value of approximately 6 dB, followed by NL3, NL5, and NL6 (Figs. 7d, f, and g, respectively), which offer

(a)

(b)
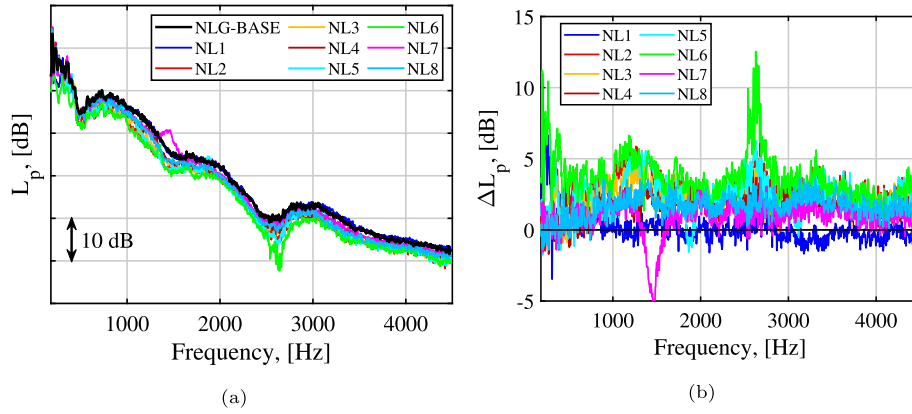
Fig. 9. (a) Narrowband spectra ($\Delta f = 4$ Hz) for all LNTs and the baseline (NLG–BASE) in the *flyover* direction for $U_\infty = 60$ m/s. (b) Corresponding reduction in the sound pressure level L_p with respect to the baseline (NLG–BASE) provided by each LNT.

peak reductions between 4 to 6 dB. The fact that the combined LNTs NL5 and NL6 provide slightly lower noise reductions than the individual measure NL2 (even if both combined technologies have NL2 equipped) is remarkable and highlights the complexity of the physical mechanisms involved in LG noise. However, as will be seen in section 4.1.2, NL6 has approximately the same performance as NL2 and both NL6 and NL5 perform better than NL3. This is a more sensible result and highlights the fact that interpretation of such source maps without integration can be erroneous. The rest of the LNTs reach lower noise reductions for this frequency band. The cases NL2, NL3, and NL5 present a slight downstream shift of the main source position away from the main strut location, whereas NL4, NL6, NL7 and NL8 seem to shift the source location in the upstream direction. The case equipped with a ramp door spoiler (NL1) slightly increases the noise emissions at this frequency band, perhaps due to the interaction of the deflected flow with certain elements of the NLG.

The side array provides a clearer point of view for separating different noise sources within the acoustic source maps, although it should be noted that the wheel and the bay door closest to the array (in the $y < 0$ subspace) may shield the sound propagation of any potential noise sources behind them. Fig. 8 contains the analogous results as for Fig. 7 (i.e. a frequency of 1250 Hz and a flow velocity of 50 m/s) but from the *side* direction. In this figure, the baseline case (Fig. 8a) shows what appears to be a distributed noise source along the main strut, especially near the wheel and around the tow fitting and the steering pinions. This source location is possibly not correct, because the 3D source map for this case, see Fig. 15a, seems to indicate that the noise source is in fact located between the wheels. Hence, the apparent source location observed in these 2D source maps is perhaps due to the shielding effect of the wheel or other sound propagation effects. The best performing LNTs are in line with those observed for the *flyover* direction in Fig. 7: NL2, NL3, NL5, and NL6, managing to significantly mitigate the noise source along the main strut. As per the *flyover* case, these four LNTs are primarily located at/within the wheels and so it seems that the noise source seen in the baseline is attenuated by these wheels LNTs most probably as a result of a change in airflow at this location. The case for NL6 (Fig. 8g), however, presents an additional noise source at the front edge of the wheel bay door (or the trailing edge of the ramp door spoiler). This is most likely due to the presence of the ramp door spoiler, since a similar (although weaker) noise source is also observed in the case of NL1 (Fig. 8b). The effect of the flow deflection by the ramp door spoiler seems to also shorten the extent of the distributed noise source along the main strut and cluster the noise sources at the outer part of it. Those LNTs equipped (only) with porous materials

(NL4, NL7, and NL8) do provide some noise mitigation, but considerably lower, even though components of them are also located between the wheels.

4.1.2. Frequency spectra

This section discusses the frequency spectra obtained by integrating the EHR–CLEAN-SC 2D source maps within the ROIs shown in section 4.1.1 for the *flyover* and the *side* directions, respectively. The noise reductions are presented as relative values with respect to the baseline case (NLG–BASE). Therefore, the parameter $\Delta L_p = L_{p,\text{baseline}} - L_{p,\text{NLi}}$ is used, where $L_{p,\text{baseline}}$ represents the noise levels of the baseline case, and $L_{p,\text{NLi}}$ those of the ith LNT, with i $= 1 \ldots 8$. In this manner, $\Delta L_p > 0$ corresponds to a noise reduction, and *vice versa*.

Flyover direction The integrated narrowband spectra for the *flyover* direction for each NLG configuration for $U_\infty = 60$ m/s are presented in Fig. 9a. The spectra at other flow velocities presented very similar trends. In general, the noise signature of all NLG configurations is mostly broadband, except for a few tonal components at the lowest frequencies. The respective narrowband noise reductions provided by each LNT with respect to NLG–BASE are shown in Fig. 9b, where it can be observed that the aforementioned low–frequency tones are effectively suppressed by NL1 and NL6. In general, all LNTs provide a fairly constant ΔL_p throughout the frequency range considered, except for frequencies close to 2700 Hz, for which noise reductions up to 12 dB are reported by NL6. Moreover, it looks like NL7 (perforated fairings with the higher porosity) produces a hump approximately at 1400 Hz that is not observed for its lower porosity counterpart NL4.

In order to have an easier readability of the noise reductions achieved, Fig. 10 contains the ΔL_p values for the *flyover* direction (i.e. as measured by the top array) expressed in one–third-octave bands for the three flow velocities. The case NL6 (NL1 + NL2 + NL3) outperforms the rest of LNTs throughout the whole frequency range and provides average noise reductions of about 6 dB for $U_\infty = 40$ m/s and 50 m/s, and 4 dB for $U_\infty = 60$ m/s. Interestingly, for some frequency bands, NL6 provides higher ΔL_p values than the summation of the individual LNTs that it consists of, showing that, in some particular cases, the technologies can be mutually beneficial [9]. However, in other instances the noise reduction provided by combined LNTs is below the sum of the individual benefits and, sometimes, even below than that of an individual treatment, such as in the aforementioned example of NL2 performing better than NL5 and NL6 at 50 m/s and 1250 Hz for the *flyover* direction. This confirms that, due to installation effects, the performance of combined LNTs cannot simply be expected to be a linear
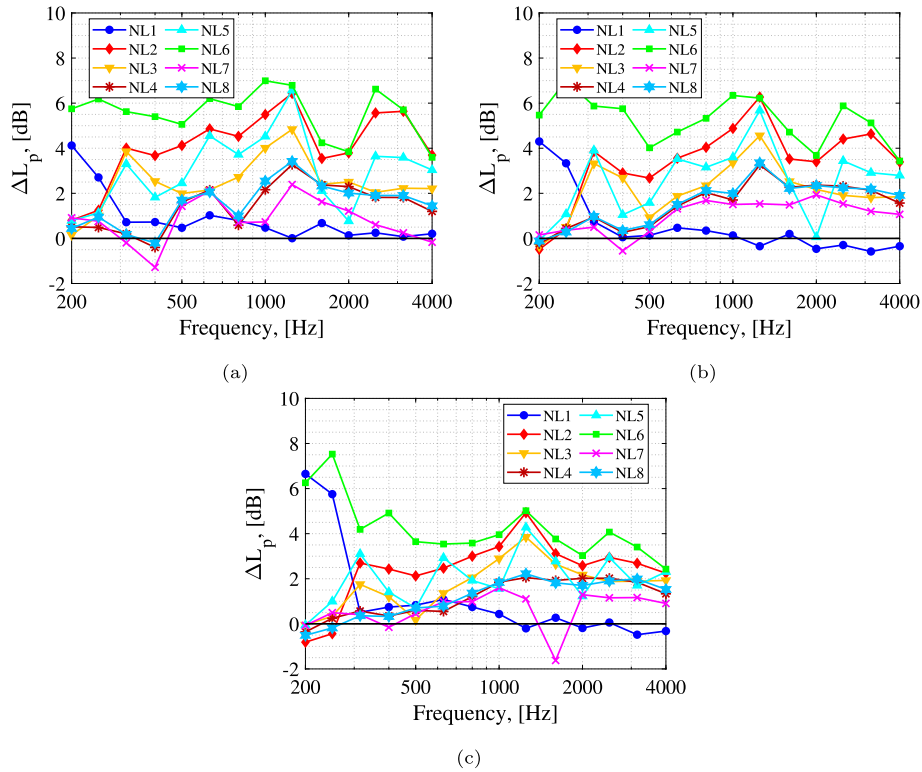
Fig. 10. Reduction in the sound pressure level L_p with respect to the baseline (NLG–BASE) provided by each LNT in the *flyover* direction as one–third–octave band spectra for (a) $U_\infty = 40$ m/s, (b) $U_\infty = 50$ m/s, and (c) $U_\infty = 60$ m/s.

sum of the individual effects. The ramp door spoiler (NL1) offers large noise reductions (up to 6 dB) for frequencies lower than 300 Hz, because the targeted noise sources by this LNT are dominant in that frequency range, such as those generated from the wheel bay shear layer. Hence, for higher frequencies, no relevant noise reduction is achieved. The measure consisting of a solid fairing at the wheel axle (NL2) achieves its best performance at 1250 Hz (up to 6 dB reduction) and presents a similar behaviour as NL6, especially for frequencies above 500 Hz, although with slightly lower ΔL_p values. This LNT also shows a low–frequency penalty around 200 Hz for the higher velocities. NL3 (wheel hub caps) follows a similar trend as NL2 but with lower ΔL_p values, especially for the case with $U_\infty = 40$ m/s. The first perforated fairing (NL4) achieves a poorer performance than the solid fairing case (NL2) with average noise reductions around 2 dB for the three flow velocities, for frequencies higher than 1 kHz. These values agree with the findings of Murayama et al. in their computational study [48]. The fairing with an alternative perforated material with higher percentage porosity (NL7) performs considerably worse than the less porous case of NL4, and even increases the noise emissions at 400 Hz for $U_\infty = 40$ m/s and 50 m/s, and at 1600 Hz for $U_\infty = 60$ m/s. NL8 (perforated fairing only at the wheel axle) essentially offers the same results as NL4 (fairing with the same perforated material but covering multiple regions of the NLG), but still considerably poorer performance than the solid fairing (NL2). This indicates that the perforated fairing is most effective at the wheel axle and that the rest of the fairings could be removed with the consequent save in weight and complexity. Lastly, the other LNT that combines several technologies (NL5 = NL2 + NL3 + NL4) provides acceptable results, but comparably lower noise reductions than NL2 when used alone.

Side direction The noise emissions in the *side* direction for each NLG configuration for $U_\infty = 60$ m/s are depicted in Fig. 11a as

narrowband spectra. In general, the noise levels measured in this direction are higher than those in the *flyover* direction for most of the frequency range. Similar low–frequency tones are observed in this case. The noise reductions achieved by each LNT are presented in Fig. 11b, where the low–frequency tones are again greatly attenuated by NL1 and NL6. Overall, considerably lower noise reductions are reported in this direction compared to the *flyover* one.

The noise reductions achieved by the LNTs on the *side* direction as measured by the side array expressed in one–third–octave bands are depicted in Fig. 12. As aforementioned, considerably lower noise reductions are obtained in this case, compared to the *flyover* direction. In essence, the same conclusions drawn before from Fig. 10 still hold for the *side* direction:

- NL6 is the best performing LNT over the whole frequency range.
- NL1 only reduces the noise emitted at low frequencies and its performance improves (in relative terms) when increasing the flow velocity.
- The solid fairing at the wheel axle (NL2) performs better than the perforated ones (NL4, NL7 and NL8), although the difference is smaller in this case.
- Most wheel–located LNTs, seem to perform best at the 315 Hz, 630 Hz and 1.25 kHz centred one–third–octave bands supporting strongly that the wheels generate noise at these frequencies as discussed at the beginning of section 4.
- Most LNTs (except for NL1) seem to provide their maximum noise reductions at 1.25 kHz for the three flow velocities.

Referring to Figs. 10 and 12, it can be noted that there tends to be a moderate decrease in the efficiency of the LNTs with increasing flow velocity. Taking NL6 as an example, for the *flyover*
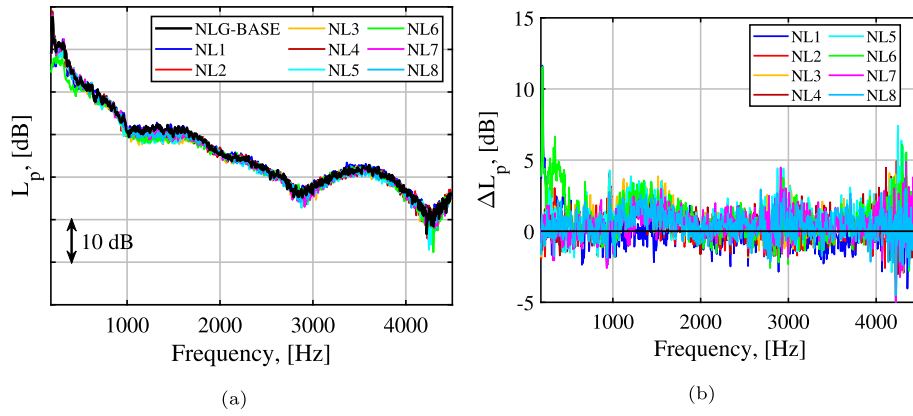
Fig. 11. (a) Narrowband spectra ($\Delta f = 4$ Hz) for all LNTs and the baseline (NLG–BASE) in the *side* direction for $U_\infty = 60$ m/s. (b) Corresponding reduction in the sound pressure level L_p with respect to the baseline (NLG–BASE) provided by each LNT.
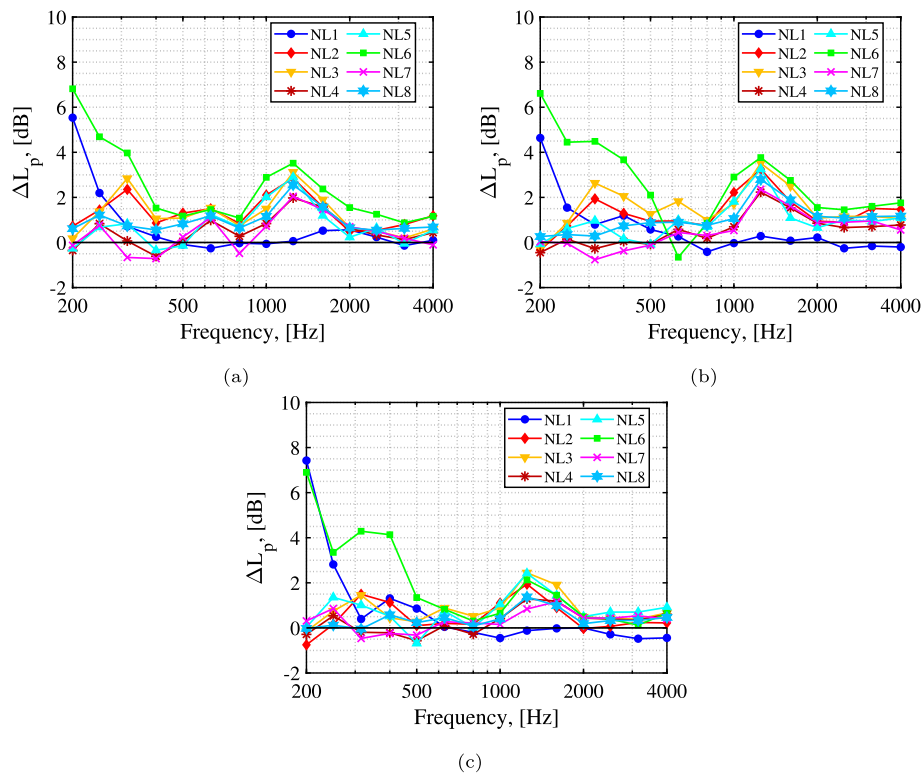

Fig. 12. Reduction in the sound pressure level L_p with respect to the baseline (NLG–BASE) provided by each LNT in the *side* direction as one–third–octave band spectra for (a) $U_\infty = 40$ m/s, (b) $U_\infty = 50$ m/s, and (c) $U_\infty = 60$ m/s.

direction the noise reduction decreases from 6.9 dB to 6.8 dB to 5 dB with increasing velocity (40 m/s, 50 m/s, and 60 m/s). For the *side* direction the noise reduction decreases from 3.5 dB at 40 m/s to 2.2 dB at 60 m/s with a slight increase to 3.8 dB at 50 m/s. In contrast, NL1 increases in efficiency with increasing flow velocity with 4.1 dB, 4.3 dB and 6.7 dB being the noise reduction attained with increasing velocity for the *flyover* direction, for example. A similar trend is observed in the *side* direction, which seems to indicate that those noise sources increase in magnitude with increasing flow velocity and also that their behaviour is almost omnidirectional in nature, being equally measurable in both directions.

At first inspection, this may seem to be counter–intuitive as if it is assumed that aerodynamic noise increases with U_∞^6, or sometimes with U_∞^7 at higher frequencies due to small features as

discussed by Guo et al. [69] and Bennett et al. [24], then one might expect the efficiency of the LNTs to increase with velocity due to an increasing noise source. However, as discussed by Casalino et al. [70] significant NLG noise is generated as a result of narrowband acoustic modes between the wheels related to the rims being excited by the flow. This is considered to be a significant noise source in our case as it was examined in a previous paper on the same experimental rig [24] and in this work it is supported by the fact that the solid wheel axle fairing (NL2) and the hubcaps (NL3) are the most efficient LNTs for the wheels. Thus, it would not be expected that these noise sources would, increase significantly with increasing flow speed and the decreasing LNT efficiency could be due to the noise over the top and bottom of the wheels increasing as U_∞^6 beginning to dominate these sources.
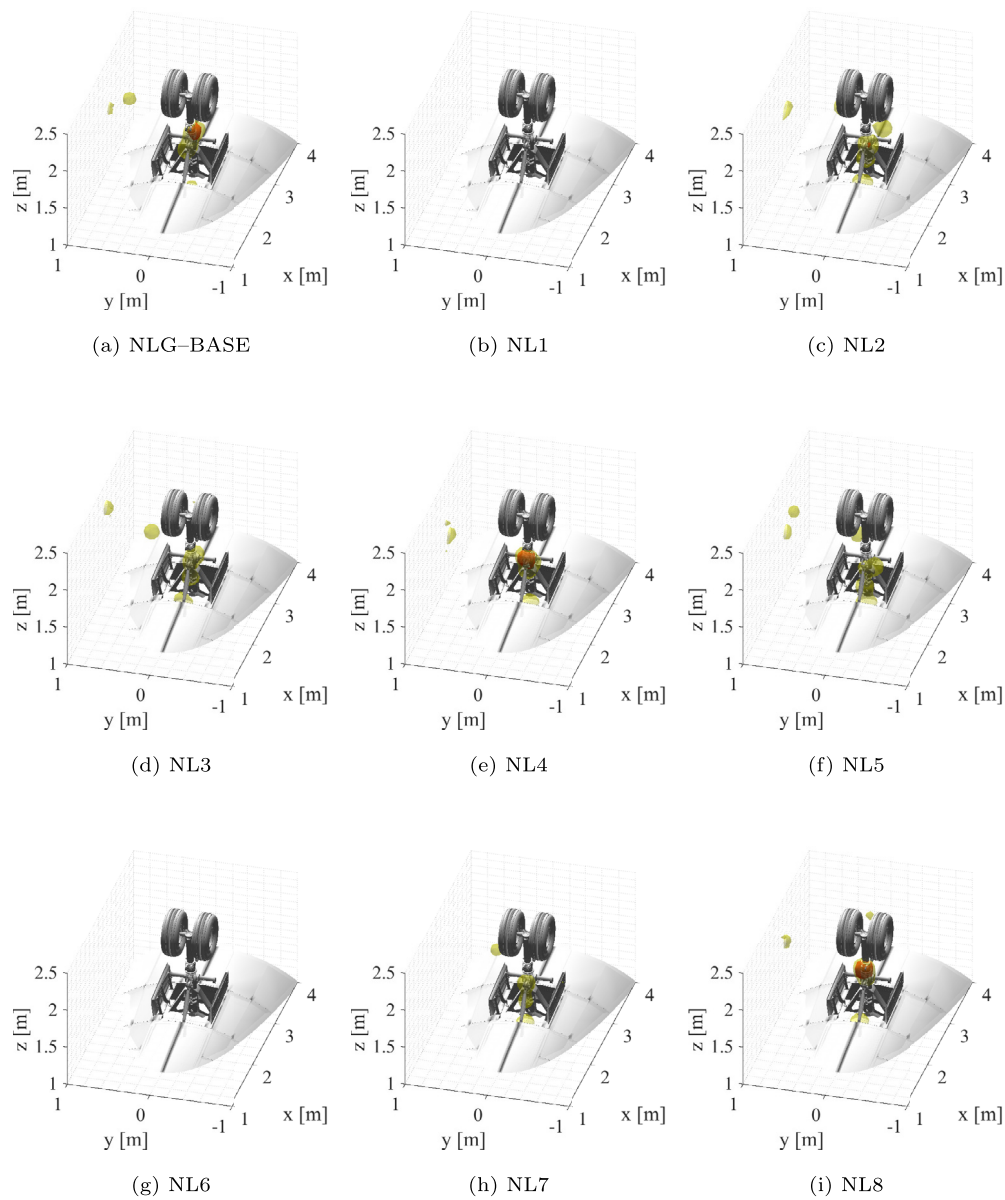
Fig. 13. Three–dimensional EHR–CLEAN–SC source maps for the one–third–octave–band centred at 200 Hz and $U_\infty = 50$ m/s. The reference case NLG–BASE is shown in subfigure (a) and subfigures (b–i) correspond to the cases NL1–NL8, respectively. The values shown are visualized as isocontours 3 dB (in red) and 6 dB (in yellow) below the peak value of the reference case (NLG–BASE).

4.2. Three–dimensional results

The two–dimensional source maps presented in section 4.1.1 provide some insight on the location of the noise sources within the NLG model, but it is challenging to identify the exact NLG elements generating the noise in each case, since both points of view have their own limitations. In addition, it is conceivable that both of these arrays may be on the same dipolar nodal plane and thus will not be sensitive to certain noise sources with such radiation patterns. The 3D acoustic mapping technique explained in section 3.2 aims at solving this issue by combining the results of the top, side, and front microphone arrays in a multiplicative approach, benefiting from their different points of view. This way, the typically poorer resolution in the directions normal to each array's plane is partially mitigated. Based on the observations made on the integrated spectra of Figs. 10 and 12 the examples presented below correspond to a flow velocity of 50 m/s and one–third–octave–bands centred at 200 Hz, 315 Hz and 1250 Hz be-

cause those frequencies showed the highest noise reductions for most of the LNTs considered. However, it was noticed that performance is better for different LNTs, highlighting the fact that the LNTs address different noise sources at different frequencies. Acoustic imaging at these frequency bands therefore helps to identify exactly which sources are being addressed. The 50 m/s test point was chosen so that results can be compared with those from earlier publications [13,24]. The relative L_p values shown are visualized as isocontours 3 dB (in red) and 6 dB (in yellow) below the peak value of the reference case (NLG–BASE).

Fig. 13 illustrates this approach for the 200 Hz case. The reference case (Fig. 13a) shows that the noise is mostly generated around the lower joint arm and the junction between the steering pinions and the main strut, i.e. not between the wheels, which explains why the wheel–located LNTs are not effective at this frequency. The weaker sources away from the NLG model present in some of the source maps are due to the poorer spatial resolution of the arrays at low frequencies. Consistent with the findings of
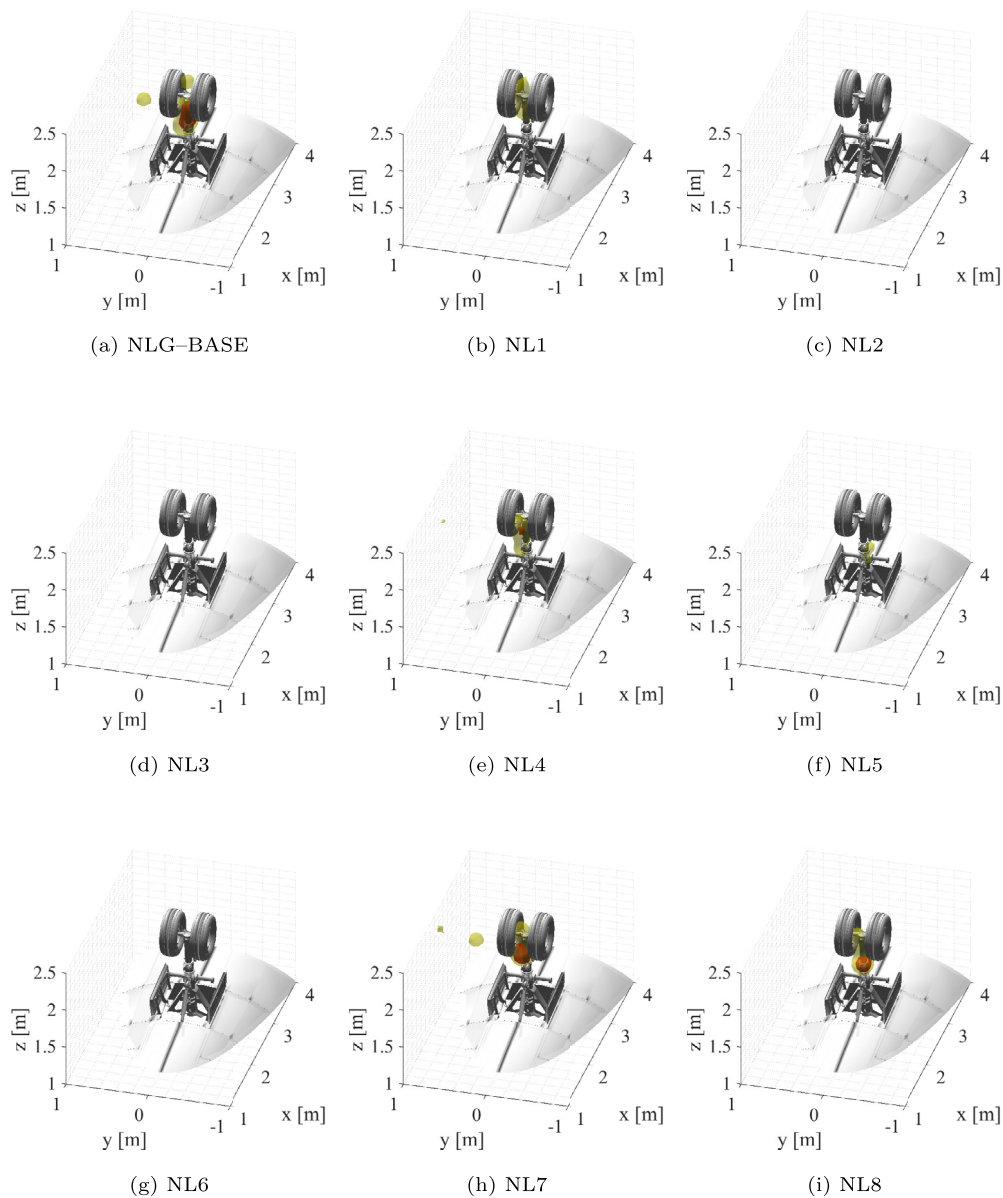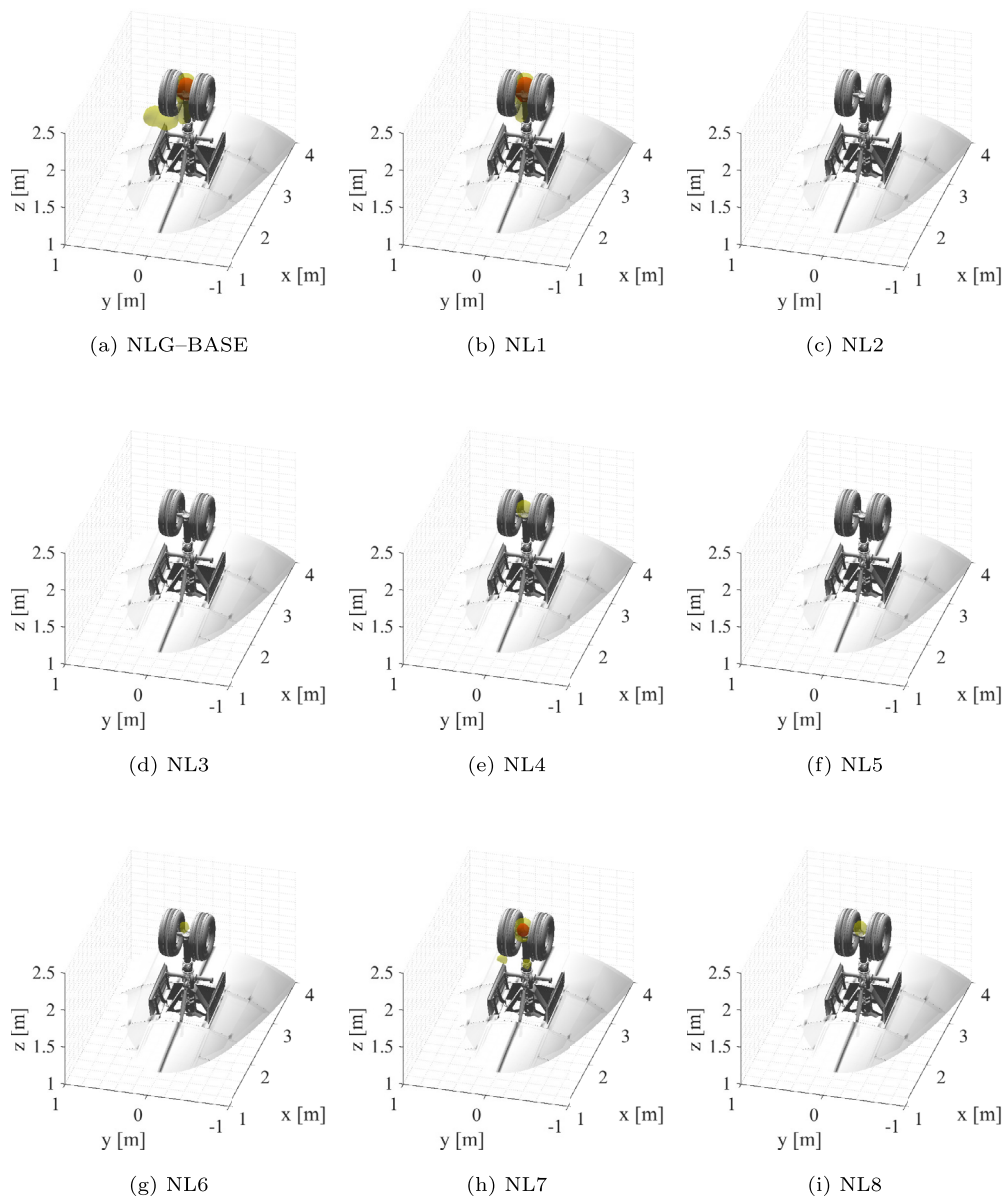
Fig. 14. Three-dimensional EHR–CLEAN–SC source maps for the one–third–octave–band centred at 315 Hz and $U_\infty = 50$ m/s. The reference case NLG–BASE is shown in subfigure (a) and subfigures (b–i) correspond to the cases NL1–NL8, respectively. The values shown are visualized as isocontours 3 dB (in red) and 6 dB (in yellow) below the peak value of the reference case (NLG–BASE).

section 4.1.2, the cases equipped with a ramp door spoiler (NL1 and NL6) completely remove that noise source (in this dynamic range), most likely due to the flow deflection. Other LNTs such as NL2, NL3, NL5 and NL7 provide smaller noise reductions. Two of the technologies equipped with porous materials (NL4 and NL8) offer a poorer performance and even increase the noise emissions slightly.

For the frequency of 315 Hz (see Fig. 14) the baseline configuration shows a cluster of noise sources along the outer part of the main strut until the junction with the wheel axle, see Fig. 14a. In this case, those LNTs equipped of solid fairings (NL2, NL5 and NL6) and wheel hub caps (NL3) considerably decrease the strength of the aforementioned noise source. The technologies consisting of porous fairings (NL4, NL7 and NL8), on the other hand, do not provide a good performance for this frequency band. Lastly, NL1 also achieves a notable noise reduction (perhaps due to the flow deflection by the ramp door spoiler) but smaller than those by NL2, NL5, and NL6.

Lastly, the source maps corresponding to the frequency of 1250 Hz are depicted in Fig. 15. For the baseline configuration (Fig. 15a) the main noise source is now located at the middle point of the wheel axle (between both wheels). Once again the LNTs equipped of solid fairings (NL2, NL5 and NL6) and wheel hub caps (NL3) manage to successfully reduce the noise levels measured. NL4 and NL8 provide an almost identical performance for this frequency band, confirming again that the perforated fairings are most effective when applied at the wheel axle. The case with a fairing made of a more porous material (NL7) performs considerably worse than the other material option. Lastly, the ramp door spoiler of NL1 barely modifies the baseline's source distribution, since this frequency is out of the intended range of this LNT.

In general, 3D source maps have the added value of offering a more precise and global assessment of the location of complex noise sources within a system by combining different points of view (in this case top, side and front). An example of this was

Fig. 15. Three–dimensional EHR–CLEAN–SC source maps for the one–third–octave–band centred at 1250 Hz and $U_\infty = 50$ m/s. The reference case NLG–BASE is shown in subfigure (a) and subfigures (b–i) correspond to the cases NL1–NL8, respectively. The values shown are visualized as isocontours 3 dB (in red) and 6 dB (in yellow) below the peak value of the reference case (NLG–BASE).

the case of the 3D source maps of Figs. 15a and b, compared to the misleading 2D source maps of Figs. 8a and b. Thus, 3D source maps should be employed in combination with the 2D source maps obtained by the individual planar arrays, since those provide an easier way to determine the noise levels in the emission directions of interest, as explained section 4.1.2.
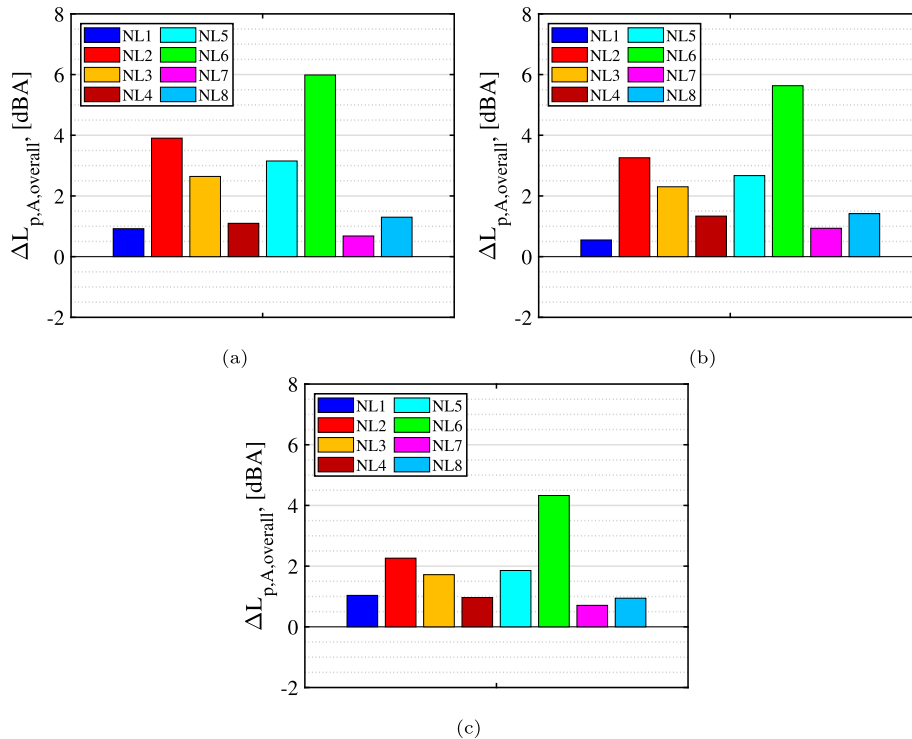
4.3. Overall noise reduction

The acoustic imaging results of sections 4.1.1 and 4.2 demonstrate that the NLG is a complex arrangement of sound sources, and that whereas the LNTs target an individual source and may reduce its level, this may not strongly affect the overall noise level as there are potentially multiple other sources of similar magnitude on different section of the landing gear.

In noise assessment applications, it is common to employ sound metrics that consider the overall frequency spectra. Given the strong low–frequency content of the noise signature of the NLG

model tested [71], it was decided to apply A–weighting to the integrated spectra, in order to highlight the relevance of the obtained noise reductions by the LNTs. Therefore, the $\Delta L_{p,A,overall}$ metric was used, in a similar way as in section 4.1.2: $\Delta L_{p,A,overall} = L_{p,A,overall,baseline} - L_{p,A,overall,NLi}$. As before, $\Delta L_{p,A,overall} > 0$ represents a noise reduction. Additionally, the D–weighted results ($\Delta L_{p,D,overall}$) are also examined, since this weighting filter was especially developed for aircraft noise measurements and is more representative of the effective perceived noise level (EPNL) metric used for aircraft certification [1]. The overall values were obtained by integrating the spectra presented in Figs. 10 and 12 within the frequency range of interest (200 Hz to 4 kHz).

4.3.1. Flyover direction

The overall A–weighted noise reductions obtained by each LNT in the *flyover* direction are presented as bar plots in Fig. 16. Not surprisingly, similar findings are observed as when analyzing the frequency spectra in section 4.1.2: NL6 (NL1 + NL2 + NL3) is the

Fig. 16. Reduction in the A–weighted overall sound pressure level $L_{p,A,overall}$ with respect to the baseline (NLG–BASE) provided by each LNT in the *flyover* direction for (a) $U_\infty = 40$ m/s, (b) $U_\infty = 50$ m/s, and (c) $U_\infty = 60$ m/s.

best performing LNT, achieving overall noise reductions of 6 dBA for $U_\infty = 40$ m/s and 50 m/s, and 4 dBA for 60 m/s. NL2 (solid wheel axle fairing) is the best performing individual LNT (with noise reductions up to 4 dBA) followed by NL3 (wheel hub caps), which achieves similar noise reductions as the combined technology NL5 (NL2 + NL3 + NL4). Overall, this indicates that simply adding as many LNTs as possible might be counterproductive, even when those LNTs have proven to have favourable individual effects. Since NL1 (ramp door spoiler) mostly reduces the noise emissions at low frequencies only and those are heavily reduced by the A–weighting, it only achieves $\Delta L_{p,A,overall}$ values of around 1 dBA. As mentioned in section 4.1.2, the additional treated regions of NL4 compared to the perforated fairing only applied to the wheel axle (NL8) do not provide any benefit. Lastly, the fairing with higher porosity (NL7) performs slightly worse than the less porous cases (NL4 and NL8). In general lower noise reductions are reached by all LNTs as the velocity increases, which can condition the performance achieved in case higher approach velocities are employed. Thus, wind–tunnel experiments at higher flow velocities would be of high interest.

In general, the D–weighted noise reductions achieved by all the LNTs (see Fig. 17) are slightly lower values than the A–weighted ones, except for NL1 and NL6 which achieve slightly higher levels because their reductions at low frequencies are more relevant in the computation of $\Delta L_{p,D,overall}$.

4.3.2. Side direction

Similar trends are observed for the case of the *side* direction see Fig. 18, although with considerably lower values. NL6 in this case only reaches overall noise reductions of 3 dBA and the rest of the LNTs also provide a poorer performance. Only NL1 seems to maintain similar values as in the *flyover* direction.

As for the *flyover* direction, all LNTs provide lower D–weighted noise reductions than the A–weighted ones, except for NL1 and NL6, see Fig. 19).

4.4. Directivity in the polar direction

The side linear array allows for a simple study of the directivity pattern that the LNTs present for their noise reductions. The same $\Delta L_{p,A,overall}$ metric as for Figs. 16 and 18 is employed, although this time the data used for the analysis does not come from the integration of acoustic source maps, but rather from the acoustic signal of the individual microphones of the side linear array. It should be noted that the use of single microphones is more sensitive to the background noise inside of the wind–tunnel facility, as the separation of noise sources is not possible as with microphone arrays. In addition, the side linear array has a sideline angle ϕ of 81°, see Fig. 2b. These two aspects are the reason why the noise reduction values presented in this section do not precisely correspond to those observed in Figs. 16 and 18.

As aforementioned, the presence of the shear layer limits the effective measurable range of polar emission angles corrected for sound convection [32]. Therefore, the available range for θ extends from approximately 35° to 145° for $U_\infty = 40$ m/s and 50 m/s, and from 35° to 110° for $U_\infty = 60$ m/s. Fig. 20 depicts the $\Delta L_{p,A,overall}$ values for all flow velocities. The results observed are qualitatively consistent with those of Figs. 16 and 18: NL6 is the best performing LNT, followed by NL2, and the noise reductions decrease when the flow velocity increases. In general, all the LNTs tested show an almost omnidirectional pattern in their noise reductions.

5. Conclusions

This manuscript has investigated the acoustic performance of several low–noise technologies (LNTs) applied to a full–scale nose landing gear (NLG) in open–jet wind–tunnel measurements. The LNTs analyzed were selected within the European Clean–Sky programme and the ALLEGRA project and were highly realistic and at a medium to high technology readiness level, allowing them to be applied to actual aircraft in the near future. There were four
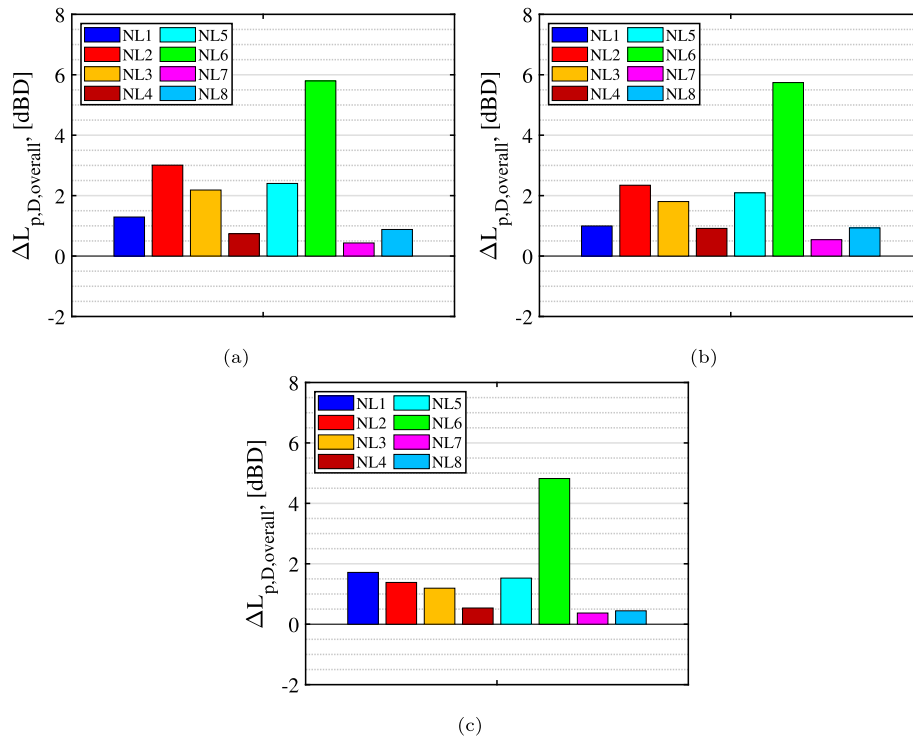
Fig. 17. Reduction in the D–weighted overall sound pressure level $L_{p,D,overall}$ with respect to the baseline (NLG–BASE) provided by each LNT in the *flyover* direction for (a) $U_\infty = 40$ m/s, (b) $U_\infty = 50$ m/s, and (c) $U_\infty = 60$ m/s.
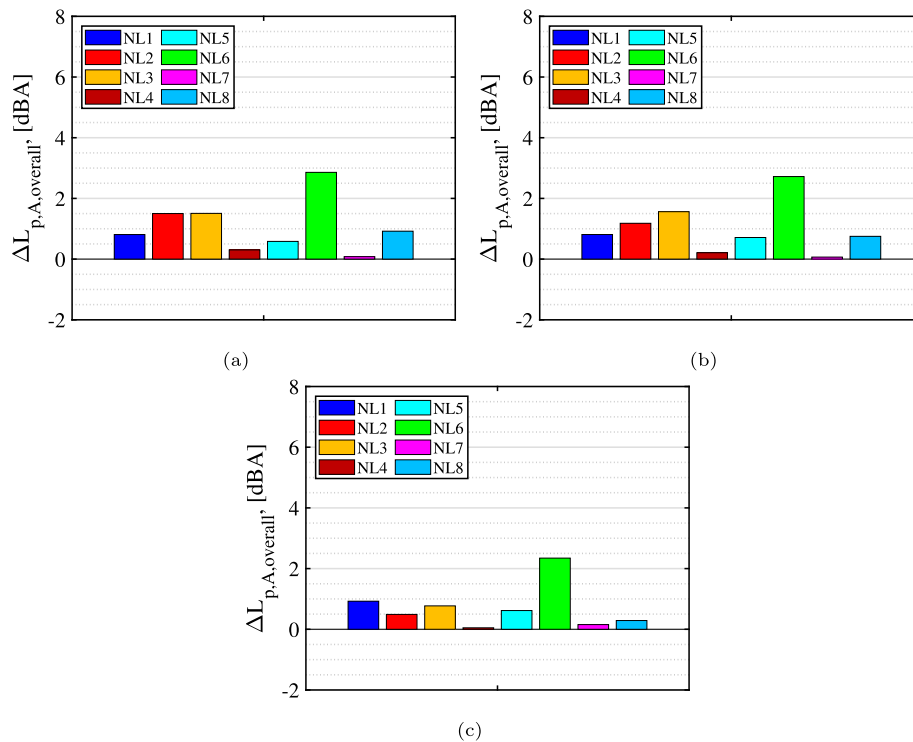

Fig. 18. Reduction in the A–weighted overall sound pressure level $L_{p,A,overall}$ with respect to the baseline (NLG–BASE) provided by each LNT in the *side* direction for (a) $U_\infty = 40$ m/s, (b) $U_\infty = 50$ m/s, and (c) $U_\infty = 60$ m/s.

main low–noise concepts tested experimentally, namely a ramp door spoiler (NL1), a solid wheel axle fairing (NL2), wheel hub caps (NL3), and multiple perforated fairings (NL4). Combinations and small variations of some of these LNTs were also investigated.

The acoustic signature of the NLG baseline model and the configurations equipped with LNTs were measured by four different microphone arrays, which allowed the study of the noise emissions in the *flyover* and *side* directions, as well as the use of 3D acoustic imaging techniques. This technique was proven very useful for determining the precise location of the noise sources within the NLG, compared to the typical 2D source maps as visibility between the wheels and doors could be obtained as well as including
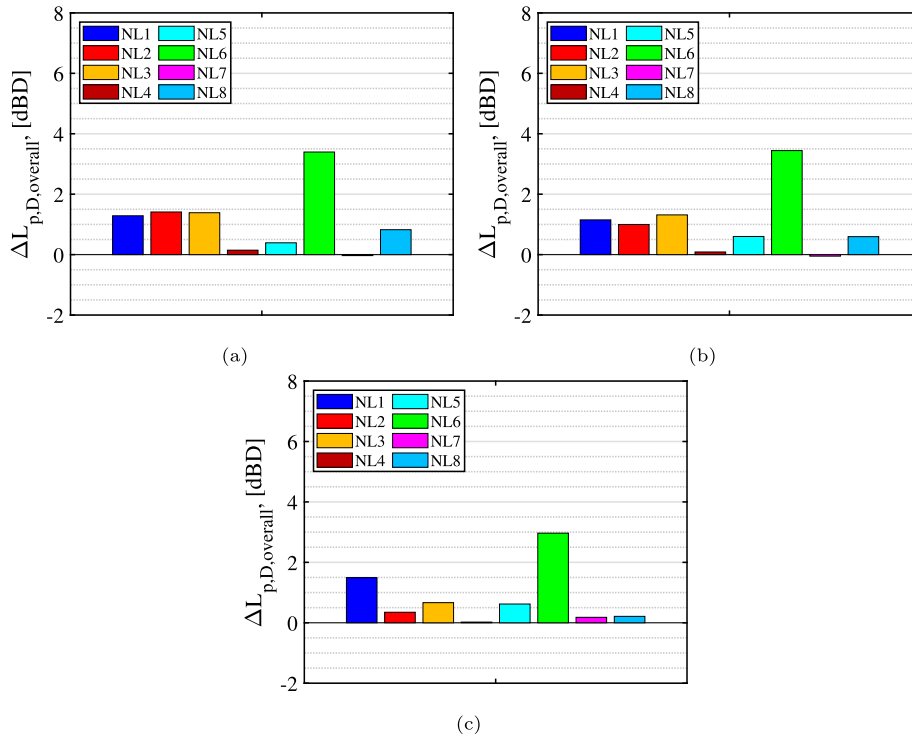
Fig. 19. Reduction in the D–weighted overall sound pressure level $L_{\text{p,D,overall}}$ with respect to the baseline (NLG–BASE) provided by each LNT in the *side* direction for (a) $U_\infty = 40$ m/s, (b) $U_\infty = 50$ m/s, and (c) $U_\infty = 60$ m/s.
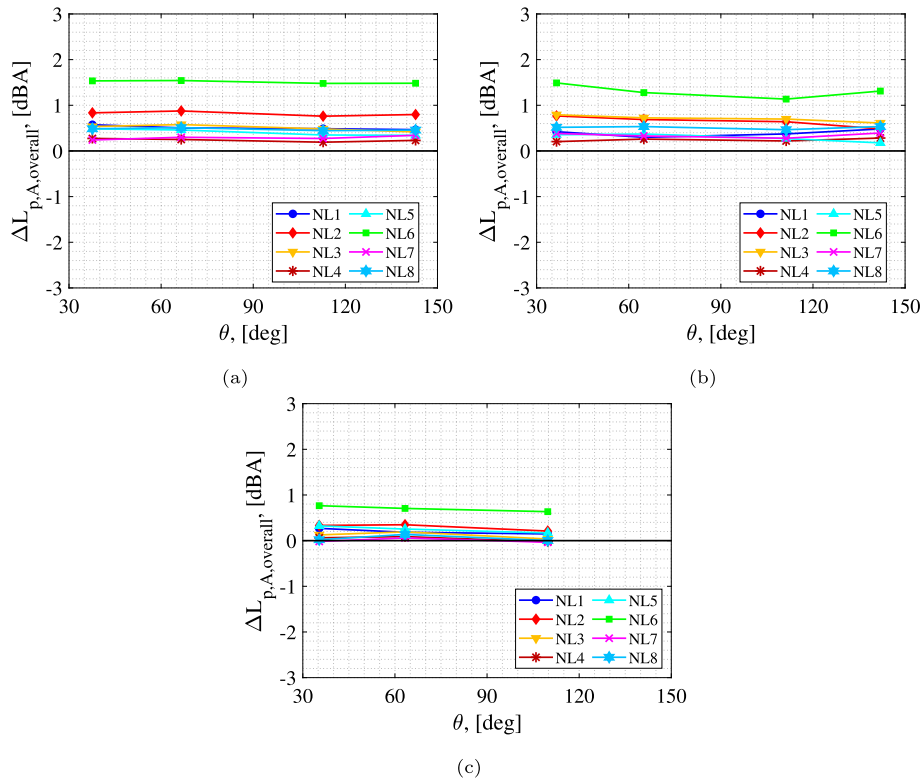

Fig. 20. Reduction in the A–weighted overall sound pressure level $L_{\text{p,A,overall}}$ with respect to the baseline (NLG–BASE) provided by each LNT for different polar emission angles θ as measured by the side linear array for (a) $U_\infty = 40$ m/s, (b) $U_\infty = 50$ m/s, and (c) $U_\infty = 60$ m/s.

extra data from the front radiation direction. Depending on the frequency, it was found that for the baseline NLG, the wheel axle, the main strut, and the tow fitting were the elements generating the highest noise levels.

The LNTs considered are designed to mitigate noise generation at different locations of the NLG system. The ramp door spoiler (NL1) achieved large noise reductions (more than 6 dB) at low frequencies (around 200 Hz). The solid wheel axle fairing (NL2)

was the best performing LNT applied individually, offering overall noise reductions between 2 and 6 dBA, particularly in the *flyover* direction and peaking at frequencies which correspond to previously determined wheel noise source frequencies. The wheel hub caps (NL3) presented similar but slightly lower noise reductions than NL2 (2 to 4 dBA). Regarding the perforated fairings (NL4), it was found that the wheel axle (NL8) is the most effective location for their application and that fairings with a larger porosity and hole size (NL7) offered slightly poorer results. Given the high complexity of porous materials for aeroacoustic applications, however, these findings are not enough to induce any design criteria, and more research on this topic is recommended.

Since each LNT acts on a different region of the NLG system, they are well suited to being applied in combination. It was found that joining the ramp door spoiler (NL1), the solid wheel axle fairing (NL2), and the wheel hub caps (NL3) into a combined LNT (denoted as NL6) offered the best global results, with overall noise reductions between 4 and 7 dBA, showing a mutually beneficial union of LNTs. The other combined technology considered (NL5), consisting of the solid wheel axle fairing (NL2), the wheel hub caps (NL3), and the multiple perforated fairings (NL4), however, did not always outperform the individual constituent LNTs, indicating that certain combinations of LNTs might be counterproductive. This fact highlights again the complexity involved in the design of optimal LNTs.

In general, all the LNTs considered showed a better performance in the *flyover* direction than in the *side* emission direction, and slightly lower noise reductions were achieved when increasing the flow speed from 40 m/s to 60 m/s. NL1 and NL6 are exceptions to these comments. Overall, conducting wind–tunnel experiments at higher flow velocities would be of high interest to evaluate this trend and more representative results for actual flight conditions. A simple directivity study in the polar emission direction showed that none of the noise reductions offered by any of the LNTs have a pronounced radiation pattern along this particular arc.

Declaration of competing interest

The authors declare that they have no known competing financial interests or personal relationships that could have appeared to influence the work reported in this paper.

Acknowledgements

References

[1] G. Ruijgrok, Elements of Aviation Acoustics, second edition, VSSD, Vereniging voor Studie- en Studentenbelangen te Delft, Delft, the Netherlands, ISBN 90-6275-899-1, 2007, https://repository.tudelft.nl/islandora/object/uuid:e4589b31-ffa3-4a5d-9400-1e2b446f60f3/?collection=research.

[2] ACARE – Strategic Research & Innovation Agenda, Tech. Rep., 2012, https://www.acare4europe.org/sites/acare4europe.org/files/document/ACARE-Strategic-Research-Innovation-Volume-1.pdf.

[3] Flightpath 2050 Europe's Vision for Aviation, Tech. Rep., European Commission, ISBN 978-92-79-19724-6, 2012, http://ec.europa.eu/transport/sites/transport/files/modes/air/doc/flightpath2050.pdf.

[4] H.H. Heller, W.M. Dobrzynski, Sound radiation from aircraft wheel–well/landing–gear configuration, J. Aircr. 14 (8) (1977) 768–774, https://doi.org/10.2514/3.58851, http://arc.aiaa.org/doi/abs/10.2514/3.58851.

[5] W. Dobrzynski, Almost 40 years of airframe noise research: what did we achieve?, J. Aircr. 47 (2) (2010) 353–367, https://doi.org/10.2514/1.44457, http://arc.aiaa.org/doi/pdf/10.2514/1.44457.

[6] L. Bertsch, Noise Prediction within Conceptual Aircraft Design, Ph.D. thesis, DLR, Bunsenstrasse 10, 37073 Göttingen, Germany, DLR Forschungsbericht, ISRN DLR–FB–2013–20, ISSN 1434-8454, 2013, http://elib.dlr.de/84386/1/phd_thesis_lothar_bertsch.pdf.

[7] R. Merino-Martinez, L. Bertsch, M. Snellen, D.G. Simons, Analysis of landing gear noise during approach, in: 22nd AIAA/CEAS Aeroacoustics Conference, Lyon, France, May 30–June 1 2016, 2016, AIAA paper 2016–2769, http://arc.aiaa.org/doi/pdf/10.2514/6.2016-2769.

[8] R. Merino-Martinez, A. Vieira, M. Snellen, D.G. Simons, Sound quality metrics applied to aircraft components under operational conditions using a microphone array, in: 25th AIAA/CEAS Aeroacoustics Conference, Delft, the Netherlands, May 20–24 2019, 2019, AIAA paper 2019–2513, http://arc.aiaa.org/doi/pdf/10.2514/6.2019-2513.

[9] K. Zhao, P. Okolo, E. Neri, P. Chen, J. Kennedy, G.J. Bennett, Noise reduction technologies for aircraft landing gear – a bibliographic review, Prog. Aerosp. Sci. (2019), https://doi.org/10.1016/j.paerosci.2019.100589, https://www.sciencedirect.com/science/article/pii/S0376042119300338.

[10] D.B. Bliss, R.E. Hayden, Landing Gear and Cavity Noise Prediction, Tech. Rep. NASA Contractor Report CR–2714, NASA Contractor Report 2714, 1976, https://ntrs.nasa.gov/archive/nasa/casi.ntrs.nasa.gov/19760021873.pdf.

[11] Y. Li, X. Wang, D. Zhang, Control strategies for aircraft airframe noise reduction, Chin. J. Aeronaut. 26 (2) (2013) 249–260, https://doi.org/10.1016/j.cja.2013.02.001.

[12] S. Khelil, P. Bardoux, J. Godard, T. Le Garrec, J. Kennedy, G.J. Bennett, Investigation of the noise emission of a regional aircraft main landing gear bay, in: 23rd AIAA/CEAS Aeroacoustics Conference, Denver, Colorado, USA, June 5–9 2017, 2017, AIAA paper 2017–3012, http://arc.aiaa.org/doi/pdf/10.2514/6.2017-3012.

[13] E. Neri, J. Kennedy, G.J. Bennett, Bay cavity noise for full–scale nose landing gear: a comparison between experimental and numerical results, Aerosp. Sci. Technol. 72 (2018) 278–291, https://doi.org/10.1016/j.ast.2017.11.016.

[14] R. Merino-Martinez, M. Snellen, Implementation of tonal cavity noise estimations in landing gear noise prediction models, in: 26th AIAA/CEAS Aeroacoustics Conference, June 15–19 2020, Virtual Event, 2020, AIAA paper 2020–2578, http://arc.aiaa.org/doi/pdf/10.2514/6.2020-2578.

[15] D.G. Crighton, Airframe Noise. (Chapter 7 of Aeroacoustics of Flight Vehicles: Theory and Practice – Volume 1: Noise Sources), Tech. Rep. NASA Technical Memorandum 1258, NASA Reference Publication 1258, 1991, https://ntrs.nasa.gov/archive/nasa/casi.ntrs.nasa.gov/19920001380.pdf.

[16] Y. Guo, Empirical Prediction of Aircraft Landing Gear Noise, Tech. Rep. NASA TM–2005–213780, NASA, July 2005, https://ntrs.nasa.gov/archive/nasa/casi.ntrs.nasa.gov/20050209966.pdf.

[17] Y. Guo, A semi–empirical model for aircraft landing gear noise prediction, in: 12th AIAA/CEAS Aeroacoustics Conference, Cambridge, Massachusetts, USA, May 8–10 2006, 2006, AIAA paper 2006–2627, http://arc.aiaa.org/doi/pdf/10.2514/6.2006-2627.

[18] M.R. Fink, Noise component method for airframe noise, in: 4th AIAA Aeroacoustics Conference, Atlanta, Georgia, USA, October 3–5 1977, October 1977, AIAA paper 1977–1271, http://arc.aiaa.org/doi/pdf/10.2514/6.1977-1271, 1977.

[19] M.G. Smith, L.C. Chow, Validation of a prediction model for aerodynamic noise from aircraft landing gear, in: 8th AIAA/CEAS Aeroacoustics Conference, Breckenridge, Co, USA, 17–19 June 2002, 2002, AIAA paper 2002–2581, http://arc.aiaa.org/doi/abs/10.2514/6.2002-2581.

[20] Y. Yokokawa, T. Imamura, H. Ura, H. Kobayashi, H. Uchida, K. Yamamoto, Experimental study on noise generation of a two–wheel main landing gear, in: 16th AIAA/CEAS Aeroacoustics Conference, Stockholm, Sweden, 2010, AIAA paper 2010–3973, http://arc.aiaa.org/doi/pdf/10.2514/6.2010-3973.

[21] W. Dobrzynski, H. Buchholz, Full–scale noise testing on Airbus landing gears in the German Dutch Wind Tunnel, in: 3rd AIAA/CEAS Aeroacoustics Conference, Atlanta, GA, USA, May 12–14 1997, 1997, AIAA paper 1997–1597, http://arc.aiaa.org/doi/pdf/10.2514/6.1997-1597.

[22] R. Merino-Martinez, E. Neri, M. Snellen, J. Kennedy, D.G. Simons, G.J. Bennett, Analysis of nose landing gear noise comparing numerical computations, prediction models and flyover and wind–tunnel measurements, in: 24th AIAA/CEAS Aeroacoustics Conference, Atlanta, Georgia, USA, June 25–29 2018, 2018, AIAA paper 2018–3299, http://arc.aiaa.org/doi/pdf/10.2514/6.2018-3299.

[23] Green Regional Aircraft (GRA), https://www.cleansky.eu/green-regional-aircraft-gra. (Accessed November 2019).

[24] G.J. Bennett, E. Neri, J. Kennedy, Noise characterization of a full-scale nose landing gear, J. Aircr. 55 (6) (2018) 2476–2490, https://doi.org/10.2514/1.C034750.

[25] E. Neri, J. Kennedy, G. Bennett, Characterization of low noise technologies applied to a full scale fuselage mounted nose landing gear, in: Proceedings of the Internoise 2015/ASME NCAD Meeting, San Francisco, CA, USA, August 9–12 2015, American Society of Mechanical Engineers (ASME), Two Park Avenue, New York, USA, 2015, NCAD2015–5911, https://www.researchgate.net/profile/Eleonora_Neri/publication/283082549_Characterization_of_low_noise_technologies_applied_to_a_full_scale_fuselage_mounted_nose_landing_gear/links/56aa06a708aef6e05df43d32/Characterization-of-low-noise-technologies-applied-to-a-full-scale-fuselage-mounted-nose-landing-gear.pdf.

[26] E. Neri, J. Kennedy, G. Bennett, Aeroacoustic source separation on a full scale nose landing gear featuring combinations of low noise technologies, in: Proceedings of the Internoise 2015/ASME NCAD Meeting, San Francisco, CA, USA, August 9–12 2015, American Society of Mechanical Engineers (ASME), Two Park Avenue, New York, USA, 2015, NCAD2015–5912, http://www.tara.tcd.ie/bitstream/handle/2262/76095/InterNoise2015_NCAD2015-5912_downloaded%20from%20proceedings.pdf?sequence=1&isAllowed=y.

[27] W.M. Dobrzynski, B. Schöning, L.C. Chow, C. Wood, M. Smith, C. Seror, Design and testing of low noise landing gears, Int. J. Aeroacoust. 5 (3) (2006) 233–262, https://doi.org/10.1260/1475-472X.5.3.233.

[28] W.M. Dobrzynski, L.C. Chow, M. Smith, A. Boillot, O. Dereure, N. Molin, Experimental assessment of low noise landing gear component design, Int. J. Aeroacoust. 9 (6) (2010) 763–786, https://doi.org/10.1260/1475-472X.9.6.763.

[29] P.A. Ravetta, R.A. Burdisso, W.F. Ng, Noise control of landing gears using elastic membrane–based fairings, in: 13th AIAA/CEAS Aeroacoustics Conference (28th AIAA Aeroacoustics Conference), Rome, Italy, May 21–23 2007, 2007, AIAA paper 2007–3466, https://arc.aiaa.org/doi/pdf/10.2514/6.2007-3466.

[30] K. Zhao, Y. Liang, P.N. Okolo, Y. Wang, Z. Wu, G.J. Bennett, Suppression of aerodynamic noise using dual-jet air curtains combined with perforated fairings, Appl. Acoust. 158 (2020) 1–6, https://doi.org/10.1016/j.apacoust.2019.107042, https://www.sciencedirect.com/science/article/pii/S0003682X19301793?via%3Dihub.

[31] K. Zhao, S. Alimohammadi, P.N. Okolo, Y. Wang, J. Kennedy, G.J. Bennett, Aerodynamic noise reduction using dual-jet planar air curtains, J. Sound Vib. 432 (2018) 192–212, https://doi.org/10.1016/j.jsv.2018.06.036.

[32] T. Mueller, Aeroacoustic Measurements, Springer Science & Business Media, Berlin, Germany, ISBN 978-3-642-07514-8, 2002, https://books.google.com/books?hl=en&lr=&id=MU6WLXFJLWgC&pgis=1.

[33] R. Merino-Martinez, P. Sijtsma, M. Snellen, T. Ahlefeldt, J. Antoni, C.J. Bahr, D. Blacodon, D. Ernst, A. Finez, S. Funke, T.F. Geyer, S. Haxter, G. Herold, X. Huang, W.M. Humphreys, Q. Leclère, A. Malgoezar, U. Michel, T. Padois, A. Pereira, C. Picard, E. Sarradj, H. Siller, D.G. Simons, C. Spehr, A review of acoustic imaging methods using phased microphone arrays (part of the Aircraft Noise Generation and Assessment special issue), CEAS Aeronaut. J. 10 (1) (2019) 197–230, https://doi.org/10.1007/s13272-019-00383-4, https://rdcu.be/brsL2.

[34] R. Merino-Martinez, Microphone arrays for imaging of aerospace noise sources, Ph.D. thesis, Delft University of Technology, ISBN 978-94-028-1301-2, 2018, https://repository.tudelft.nl/islandora/object/uuid:a3231ea9-1380-44f4-9a93-dbbd9a26f1d6?collection=research.

[35] U. Michel, B. Barsikow, J. Helbig, M. Hellmig, M. Schüttpelz, Flyover noise measurements on landing aircraft with a microphone array, in: 4th AIAA/CEAS Aeroacoustics Conference, Toulouse, France, June 2–4 1998, 1998, AIAA paper 1998–2336.

[36] P. Sijtsma, Phased array beamforming applied to wind tunnel and fly-over tests, Tech. Rep. NLR–TP–2010–549, National Aerospace Laboratory (NLR), Anthony Fokkerweg 2, 1059 CM Amsterdam, P.O. Box 90502, 1006 BM Amsterdam, the Netherlands, December 2010, https://reports.nlr.nl/xmlui/bitstream/handle/10921/192/TP-2010-549.pdf?sequence=1.

[37] R. Merino-Martinez, M. Snellen, D.G. Simons, Functional beamforming applied to imaging of flyover noise on landing aircraft, J. Aircr. 53 (6) (2016) 1830–1843, https://doi.org/10.2514/1.C033691, http://arc.aiaa.org/doi/abs/10.2514/1.C033691.

[38] M. Snellen, R. Merino-Martinez, D.G. Simons, Assessment of noise level variability on landing aircraft using a phased microphone array, J. Aircr. 54 (6) (2017) 2173–2183, https://doi.org/10.2514/1.C033950.

[39] R. Merino-Martinez, E. Neri, M. Snellen, J. Kennedy, D.G. Simons, G.J. Bennett, Comparing flyover noise measurements to full–scale nose landing gear wind–tunnel experiments for regional aircraft, in: 23rd AIAA/CEAS Aeroacoustics Conference, Denver, Colorado, USA, June 5–9 2017, 2017, AIAA paper 2017–3006, http://arc.aiaa.org/doi/pdf/10.2514/6.2017-3006.

[40] J. Kennedy, E. Neri, G. Bennett, The reduction of main landing gear noise, in: 22nd AIAA/CEAS Aeroacoustics Conference, Lyon, France, May 30–June 1 2015, 2016, AIAA paper 2016–2900, http://arc.aiaa.org/doi/pdf/10.2514/6.2016-2900.

[41] R. Porteous, Z. Prime, C.J. Doolan, D.J. Moreau, Three–dimensional beamforming of dipolar aeroacoustic sources, J. Sound Vib. 355 (2015) 117–134, https://doi.org/10.1016/j.jsv.2015.06.030.

[42] Pininfarina website, https://pininfarina.it/en/wind-tunnel/. (Accessed November 2019).

[43] P.D. Welch, The use of fast Fourier transform for the estimation of power spectra: a method based on time averaging over short, modified periodograms, IEEE Trans. Audio Electroacoust. AU–15 (2) (1967) 70–73, https://doi.org/10.1109/TAU.1967.1161901, http://ieeexplore.ieee.org/stamp/stamp.jsp?arnumber=1161901.

[44] E. Neri, Characterisation and Reduction of Aircraft Landing Gear Noise, Ph.D. thesis, Trinity College Dublin, 2017, http://www.tara.tcd.ie/handle/2262/81876.

[45] A. Hajczak, L. Sanders, P. Druault, Landing gear interwheel tonal noise characterization with the boundary element method, J. Sound Vib. 458 (2019) 44–61, https://doi.org/10.1016/j.jsv.2019.06.010.

[46] D. Casalino, A.F.P. Ribeiro, E. Fares, S. Nölting, Lattice–Boltzmann aeroacoustic analysis of the LAGOON landing–gear configuration, AIAA J. 52 (6)

(2014) 1232–1248, https://doi.org/10.2514/1.J052365, http://arc.aiaa.org/doi/pdf/10.2514/1.J052365.

[47] T.R. Ricciardi, W.R. Wolf, R. Speth, Acoustic prediction of LAGOON landing gear: cavity noise and coherent structures, AIAA J. 56 (11) (2018) 4379–4399, https://doi.org/10.2514/1.J056957, https://arc.aiaa.org/doi/pdf/10.2514/1.J056957.

[48] M. Murayama, Y. Yokokawa, K. Yamamoto, T. Hirai, Computational study of low–noise fairings around tire–axle region of a two–wheel main landing gear, Comput. Fluids 85 (2013) 114–124, https://doi.org/10.1016/j.compfluid.2012.11.001.

[49] P. Eret, J. Kennedy, G.J. Bennett, Effect of noise reducing components on nose landing gear stability for a mid–size aircraft coupled with vortex shedding and freeplay, J. Sound Vib. 354 (2015) 91–103, https://doi.org/10.1016/j.jsv.2015.06.022.

[50] Y. Li, M. Smith, X. Zhang, Measurement and control of aircraft landing gear broadband noise, Aerosp. Sci. Technol. 23 (1) (2012) 213–223, https://doi.org/10.1016/j.ast.2011.07.009, SAGE Publications Ltd. London, United Kingdom.

[51] R. Elkoby, L. Brusniak, R.W. Stoker, M.R. Khorrami, A. Abeysinghe, J.W. Moe, Airframe noise results from the QTD II flight test program, in: 13th AIAA/CEAS Aeroacoustics Conference (28th AIAA Aeroacoustics Conference), Rome, Italy, May 21–23 2017, 2007, AIAA paper 2007–3457.

[52] M.R. Khorrami, D.P. Lockard, W.M. Humphreys Jr., P.A. Ravetta, Flight–test evaluation of airframe noise mitigation technologies, in: 24th AIAA/CEAS Aeroacoustics Conference, Atlanta, Georgia, USA, June 25–29 2018, 2018, AIAA paper 2018–2972, http://arc.aiaa.org/doi/pdf/10.2514/6.2018-2972.

[53] M.R. Khorrami, D.P. Lockard, W.M. Humphreys Jr., P.A. Ravetta, Flight–test evaluation of landing gear noise reduction technologies, in: 25th AIAA/CEAS Aeroacoustics Conference, Delft, the Netherlands, May 20–24 2019, 2019, AIAA paper 2019–2455, http://arc.aiaa.org/doi/pdf/10.2514/6.2019-2455.

[54] P.A. Ravetta, D.M. Wisda, M.R. Khorrami, T. Van de Ven, Assessment of airframe noise reduction technologies based on EPNL from flight tests, in: 25th AIAA/CEAS Aeroacoustics Conference, Delft, the Netherlands, May 20–24 2019, 2019, AIAA paper 2019–2456 http://arc.aiaa.org/doi/pdf/10.2514/6.2019-2456.

[55] A. Rubio Carpio, R. Merino-Martinez, F. Avallone, D. Ragni, M. Snellen, S. van der Zwaag, Experimental characterization of the turbulent boundary layer over a porous trailing edge for noise abatement, J. Sound Vib. 443 (2019) 537–558, https://doi.org/10.1016/j.jsv.2018.12.010.

[56] K. Boorsma, Aeroacoustic Control of Landing Gear Noise using Perforated Fairings, Ph.D. thesis, University of Southampton, 2008, https://eprints.soton.ac.uk/66081/.

[57] K. Boorsma, X. Zhang, N. Molin, Landing gear noise control using perforated fairings, Acta Mech. Sin. 26 (2) (2010) 159–174, https://doi.org/10.1007/s10409-009-0304-0.

[58] R.K. Amiet, Refraction of sound by a shear layer, J. Sound Vib. 58 (4) (1978) 467–482, https://doi.org/10.1016/0022-460X(78)90353-X.

[59] R. Merino-Martinez, G. Herold, M. Snellen, R.P. Dougherty, Assessment and comparison of the performance of functional projection beamforming for aeroacoustic measurements, in: 8th Berlin Beamforming Conference, Berlin, Germany, March 2–3 2020, GFaI, e.V., Berlin, 2020, BeBeC–2020–S7, http://www.bebec.eu/Downloads/BeBeC2020/Papers/BeBeC-2020-S07.pdf.

[60] R. Merino-Martinez, P. Sijtsma, M. Snellen, Inverse integration method for distributed sound sources, in: 7th Berlin Beamforming Conference, Berlin, Germany, March 5–6 2018, GFaI, e.V., Berlin, 2018, BeBeC–2018–S07, http://www.bebec.eu/Downloads/BeBeC2018/Papers/BeBeC-2018-S07.pdf.

[61] R. Merino-Martinez, P. Sijtsma, A. Rubio Carpio, R. Zamponi, S. Luesutthiviboon, A.M.N. Malgoezar, M. Snellen, C. Schram, D.G. Simons, Integration methods for distributed sound sources, Int. J. Aeroacoust. 18 (4–5) (2019) 444–469, https://doi.org/10.1177/1475472X19852945.

[62] P. Sijtsma, R. Merino-Martinez, A.M.N. Malgoezar, M. Snellen, High–resolution CLEAN–SC: theory and experimental validation, Int. J. Aeroacoust. 16 (4–5) (2017) 274–298, https://doi.org/10.1177/1475472X17713034, SAGE Publications Ltd. London, United Kingdom, http://journals.sagepub.com/doi/10.1177/1475472X17713034.

[63] S. Luesutthiviboon, A.M.N. Malgoezar, R. Merino-Martinez, M. Snellen, P. Sijtsma, D.G. Simons, Enhanced HR–CLEAN–SC for resolving multiple closely spaced sound sources, Int. J. Aeroacoust. 18 (4–5) (2019) 392–413, https://doi.org/10.1177/1475472X19852938.

[64] R. Merino-Martinez, S. Luesutthiviboon, R. Zamponi, A. Rubio Carpio, D. Ragni, P. Sijtsma, M. Snellen, C. Schram, Assessment of the accuracy of microphone array methods for aeroacoustic measurements, J. Sound Vib. 470 (115176) (2020) 1–24, https://doi.org/10.1016/j.jsv.2020.115176.

[65] R. Zamponi, P. Chiariotti, G. Battista, C. Schram, P. Castellini, 3D generalized inverse beamforming in wind tunnel aeroacoustic testing: application to a counter rotating open rotor aircraft model, Appl. Acoust. 163 (107229) (2020) 1–11, https://doi.org/10.1016/j.apacoust.2020.107229.

[66] E. Sarradj, Three–dimensional acoustic source mapping with different beamforming steering vector formulations, Adv. Acoust. Vib. 2012 (292695) (2012) 1–12, https://doi.org/10.1155/2012/292695.

[67] G. Battista, P. Chiariotti, M. Martarelli, P. Castellini, Inverse methods in aeroacoustic three–dimensional volumetric noise source localization and quantification, J. Sound Vib. 473 (2020) 1–26, https://doi.org/10.1016/j.jsv.2020.115208.

[68] R. Merino-Martinez, M. Snellen, D.G. Simons, Functional beamforming applied to full scale landing aircraft, in: 6th Berlin Beamforming Conference, Berlin, Germany, February 29–March 1 2016, GFaI, e.V., Berlin, 2016, BeBeC–2016–D12, http://www.bebec.eu/Downloads/BeBeC2016/Papers/BeBeC-2016-D12.pdf.

[69] Y. Guo, K.J. Yamamoto, R.W. Stoker, Experimental study on aircraft landing gear noise, J. Aircr. 43 (2) (2006) 306–317, https://doi.org/10.2514/1.11085, http://arc.aiaa.org/doi/abs/10.2514/1.11085.

[70] D. Casalino, A.F.P. Ribeiro, E. Fares, Facing rim cavities fluctuation modes, J. Sound Vib. 333 (13) (2014) 2812–2830, https://doi.org/10.1016/j.jsv.2014.01.028.

[71] R. Merino-Martinez, E. Neri, M. Snellen, J. Kennedy, D.G. Simons, G.J. Bennett, Multi–approach study of nose landing gear noise, J. Aircr. 57 (3) (2020) 517–533, https://doi.org/10.2514/1.C035655.